HIGH ORDER NUMERICAL SCHEMES FOR PDES AND APPLICATIONS TO CFD

by

HUANKUN FU

Presented to the Faculty of the Graduate School of
The University of Texas at Arlington in Partial Fulfillment
of the Requirements
for the Degree of

DOCTOR OF PHILOSOPHY

THE UNIVERSITY OF TEXAS AT ARLINGTON

December 2013

ACKNOWLEDGEMENTS

Initially, I would like to thank my research advisor and committee chairman, Dr. Chaoqun Liu, for his guidance, advice, continuous support, encouragement, patience and understanding in both academics and life throughout my four years of study. It has been a true honor to work with him.

Also, I would like to thank the other committee members, Dr. Andrzej Korzeniowski, Dr. Guojun Liao, Dr. Hristo Kojouharov, and Dr. Jianzhong Su, for their understanding and support.

I would like to thank the Department of Mathematics, for the financial support during the long semesters through Graduate Teaching Assistantships, and I would also like to thank all colleagues for making my time at the University of Texas at Arlington a great experience.

Finally, thanks to my wife, Xiaoyan Zhang, for her love, patience, understanding, kind support, encouragement, and for making this work interesting and a success. I am extremely fortunate to be so blessed. I am also extremely grateful to my family for their love and relentless unconditional support from overseas.

November 22, 2013

ABSTRACT

HIGH ORDER NUMERICAL SCHEMES FOR PDES
AND APPLICATIONS TO CFD

HUANKUN FU, Ph.D.

The University of Texas at Arlington, 2013

Supervising Professor: Chaoqun Liu

In the past two decades, many efforts have been made in developing high-order schemes with high resolution, such as compact scheme, essentially non-oscillatory scheme (ENO), weighted essentially non-oscillatory scheme (WENO).

The present dissertation comprises the analysis and numerical testing of two high order methods. The first one refers to the modification of pseudo spectral method which can be used to partial differential equations(PDEs) with non-periodic boundary conditions. The second one is in high order finite difference class and is the mixing of weighted non-oscillatory scheme and compact scheme (MWCS) with using global weights instead of local ones. Numerical tests are performed for one dimensional and two dimensional cases and results are compared with some well-established numerical schemes.

TABLE OF CONTENTS

LIST OF ILLUSTRATIONS

LIST OF TABLES

CHAPTER 1

INTRODUCTION

It is desirable for a numerical scheme to attain high-order accuracy and high resolution with limited computational resources. In the past few decades, many efforts have been made in developing high-order schemes. Examples include the compact difference schemes [1, 2, 3], essentially non-oscillatory (ENO) schemes [4, 5, 6], and their weighted ENO scheme (WENO) [7, 8, 9], discontinuous Gelerkin (DG) methods [10, 11, 12], pseudo-spectral method [13], spectral element (SE) methods [14], spectral volume methods (SVM) [15, 16], spectral difference methods (SDM) [17, 18], low dissipative high-order schemes [19], group velocity control schemes [20], and hybrid schemes [21, 22], etc.

Physical processes usually have various different length scales. In the case of flow transition and turbulence, for example, small length scales are of great interest and very sensitive to any artificial numerical dissipation. The pseudo-spectral method [13] and high order central compact scheme [1, 2] (Lele, 1992; Visbal, et al., 2002) are non-dissipative and of high-order and high-resolution, and thus are appropriate for the solution of flow transition and turbulence simulation. However, the pseudo-spectral method is neither applicable when the boundary conditions are not periodic nor when the shock is met, and the compact scheme is not feasible in many engineering applications such as shock-boundary layer interaction, shock-acoustic interaction, image process, flow in porous media, multiphase flow and detonation wave, where there is a presence of both different length scales and shocks or discontinuities.

The first problem comes for the periodic boundary conditions of PDEs when using the pseudo-spectral method. It is well known that spectral methods are a class of techniques used in applied mathematics and scientific computing to numerically solve certain PDEs. The pseudo-Spectral Method which utilizes the efficient algorithm of fast Fourier transform (FFT) to solve differential and pseudo-differential equations in spatially periodic domains. It has emerged as a powerful computational technique for the simulation of complex smooth physical phenomena, and its exponential convergence rate depends on the smoothness and periodicity of the function in the domain of interest. As is known, Fourier spectral method is a high order method and can be used to resolve the small length scales, which is particularly important for simulation of turbulence and acoustic problems because of its high resolution. Since its inception in the early 1970's, spectral methods have been extensively used to solve a lot of problems including turbulence. However, the classical pseudo-spectral method imposes a restriction on boundary conditions which must be periodic. Such a restriction cannot be applied to practical flows that usually have non-periodic boundary conditions. To overcome this problem, people did a lot of work, for example, changing the basis functions to be Chebyshev polynomials or other polynomials. In that way, one can get Chebyshev spectral method and so on, refer to [23], but they have lower resolution than the original trigonometry polynomials. Also, windows can be used to treat the boundary conditions, then the physical solution near the boundaries is obtained by a regularized dewindowing operation, and meanwhile, on the inner domain, the unmodified equations are solved, refer to [24]. There are other works which also deal with parts of the problems, like [25] through [26].

As is known, even though the function value itself (not derivative) is periodic on the boundary, the classical pseudo-spectral method may still not work. Therefore, modifying the function and making some orders of derivatives of the function to be

periodic on the boundary is very important, then this method can be used to solve PDEs with non-periodic boundary conditions with smooth solutions, which will lead to a successful expanding usage of pseudo-spectral methods. While, if the shock is met, pseudo-spectral is not applicable even when the boundary conditions are periodic, making further research is necessary. However, some compromises can still be made, which leads to another topic of this paper.

The shock can be considered as a discontinuity or a mathematical singularity. In fact, there is no classical unique solution and the derivatives are not bounded. In the near-shock region, continuity and differentiability of the governing Euler equations are lost and only the weak solution can be obtained. In fluid dynamics, it is possible to have a shock solution when considering, for instance, the supersonic regime of the Euler equations, which are hyperbolic. Hyperbolic systems can be solved taking advantage of the characteristic lines and Riemann invariants. The physics of the shock indicate that the derivative across the shock is not finite, and that the downstream region cannot influence the upstream one. In the framework of finite differences it makes no sense to use, for instance, a high order compact scheme, which takes all grid points on both sides of a shock into account for the numerical approximation of the derivatives. Apparently, the upwind strategies are more suitable than compact schemes in dealing with shocks, and indeed history has shown a great success of upwind technologies applied to hyperbolic systems. Among upwind or bias upwind schemes that are capable to capture a shock sharply, there are Godunov [27], Roe [28], MUSCL [29], TVD [35], ENO [4, 5, 6] and WENO [7, 8]. All mentioned schemes above are based on upwinding or biased upwinding technology and are well suited for hyperbolic systems. On the other hand, upwinding strategies are not desirable for solving Navier-Stokes systems, which present a parabolic behavior, and are very sensi-

tive to any numerical dissipation especially when tackling the problem of transitional and turbulent flow, where small length scales are important.

Efforts have been made in developing high-order numerical schemes with high resolution for small length scales and capability of sharply capturing the shock or discontinuity without generating visible numerical oscillations. A combination of WENO and standard central scheme is proposed in references [30, 31]. Additionally, a combination of WENO and upwinding compact scheme (UCS) is proposed by reference [33], but the mixing function is still complex and has a number of case related adjustable coefficients, which is not convenient to use.

A weighted compact scheme (WCS) is developed by reference [32]. WCS is based on the WENO [7] weighting method for evaluating several stencil candidates. However, the building block for each candidate is a Lagrange polynomial in WENO, but is a Hermite in WCS aiming to obtain higher order of accuracy with the same stencil width. In shock regions, the WCS controls the contributions of different candidate stencils to minimize the influence of candidates containing a shock or discontinuity. On the other hand, in regions with smooth solution, WCS recovers the standard compact scheme [1] to achieve high accuracy and high resolution. Numerical tests reveal that the original WCS works well in some cases such as Burgers' equation, but is not suitable for solving the Euler equations with shocks. However, the usage of derivatives calculated by compact schemes results in global dependency which is not allowed for shocks. WCS minimizes the influence of a shock-containing candidate stencil by assigning a smaller weight, but still uses all of the candidates, resulting in global dependency.

This dissertation mainly focuses on two kinds of numerical schemes. For the first one, it mainly focuses on modifying the classical Fourier spectral method to get the accurate derivative of a function which is not periodic on boundary. Instead

of using the classical Fourier spectral method directly for the problems immediately, it is necessary, by professor Chaoqun Liu's idea, to first modify and extend the original function to get a new extended function (which is probably very different from the origin function), for which classical Fourier spectral method can be easily used. After getting the derivatives of the new function, it is now easy to recover the derivative of the original function. For another one, it is necessary to overcome the drawback of the WCS, hence local dependency has to be achieved in shock areas while recovering global dependency in smooth regions. This fundamental idea leads naturally to the combination of compact and non-compact schemes, that is, to the mixed weighted compact and non-compact scheme (MWCS). The proposed scheme is to add WENO schemes to WCS so that the oscillations, which can be produced by global dependency, can be obviously prevented. Moreover, one important change is that the commonly used WENO weights and WCS weights are relocated outside the subroutine for derivatives, which was first stated by professor Chaoqun Liu, and only the weights calculated for pressure and density are used for all parameters. In such a case, the scheme is no longer a black box, the cost is reduced considerably, and the oscillations are further reduced due to the consistency of weights for all variables.

The structure of this dissertation is as follows, in Chapter 2, buffered Fourier spectral method will be introduced; In Chapter 3, details about modified weighted compact scheme will be discussed, and Chapter 4 includes conclusion for this dissertation.

CHAPTER 2

BUFFERED FOURIER SPECTRAL METHOD

2.1 Pseudo-spectral Method (PSM)

2.1.1 Fourier Interpolation

For a periodic sequence $\{x_n = 2\pi n/N, n = 0, 1, \cdots, N\}$, the function $f(x)$ can be approximated by the following Fourier interpolation as

$$I_N f = \sum\nolimits_{k=-N/2}^{N/2} \frac{\tilde{f}_k}{\bar{c}_k} e^{ikx}, \tag{2.1}$$

here, $\bar{c}_k = \begin{cases} 1, & k = -N/2+1, ..., N/2-1; \\ 2, & k = \pm N/2, \end{cases}$ and $\tilde{f}_k = \frac{1}{N}\sum_{j=0}^{N-1} f_j e^{-ikx_j}, k = -N/2,$ $..., N/2.$

2.1.2 Discrete Fourier Transform (DFT)

For a sequence $\{f(x_i)\}, i = 0, 1, \cdots, N-1$, the discrete Fourier transform (DFT) is defined as

$$\tilde{f}_k = \frac{1}{N}\sum\nolimits_{j=0}^{N-1} f(x_j) e^{-2\pi ijk/N}, k = -N/2, ..., N/2-1. \tag{2.2}$$

The inverse transform is

$$f(x_j) = \sum\nolimits_{k=-N/2}^{N/2-1} \tilde{f}_k e^{2\pi ijk/N}, j = 0, 1, ..., N-1. \tag{2.3}$$

2.1.3 PSM for Derivatives

Traditional Fourier spectral method for derivatives is based on the Fourier interpolation and use DFT/FFT to get coefficients of the DFT and then the original

function derivatives. The original function is approximated by 2.1, and hence the derivative is

$$f' = (I_N f)' = \sum_{k=-N/2}^{N/2} \frac{\tilde{f}_k}{\bar{c}_k}(ik)e^{ikx}. \tag{2.4}$$

Therefore, if we want to get f', we first use FFT to get the coefficients of DFT of f, and then multiply each of them with the corresponding number ik. After we perform the inverse DFT by FFT, the derivative is available.

2.2 Buffered Fourier Spectral Method (BFSM)

2.2.1 Introduction

The periodic boundary condition is necessary when applying standard Fourier spectral method, which is too restrictive. Even for a simple function like $y = x^2, (-1 \leq x \leq 1)$, with periodic boundary values but non-periodic boundary derivatives, results a disaster. However, most practical engineering problems have non-periodic boundary conditions. Therefore, it is very important to modify the Fourier spectral method so that it can be adopted for problems with non-periodic boundary conditions. This is the major purpose of the current part. This modified Fourier spectral method, called buffered Fourier spectral method or briefly BFSM, can be described by two steps: 1. normalization(by Huankun Fu); 2. smooth buffer extension(by Dr. Liu).

2.2.2 Smooth Buffer Extension

2.2.2.1 Problems with standard PST

Take a look at a simple example(Figure 2.1(a)), $y = x^2, (-1 \leq x \leq 1)$, to illustrate how to develop a smooth buffer extension. This simple function can be artificially extended as a periodic function with $T = 2$ as shown in Figure 2.1(b) which

uses Fourier transform. However, it is not difficult to find that the derivatives on the boundaries, i.e., at $x = -1$ and 1, the derivatives do not exist. If the traditional FFT is used to calculate the derivatives, it will present serious oscillations (Gibbs Phenomenon) (Figure 2.1(c)), but the exact derivative is $y' = 2x$ (Figure 2.1(d)).

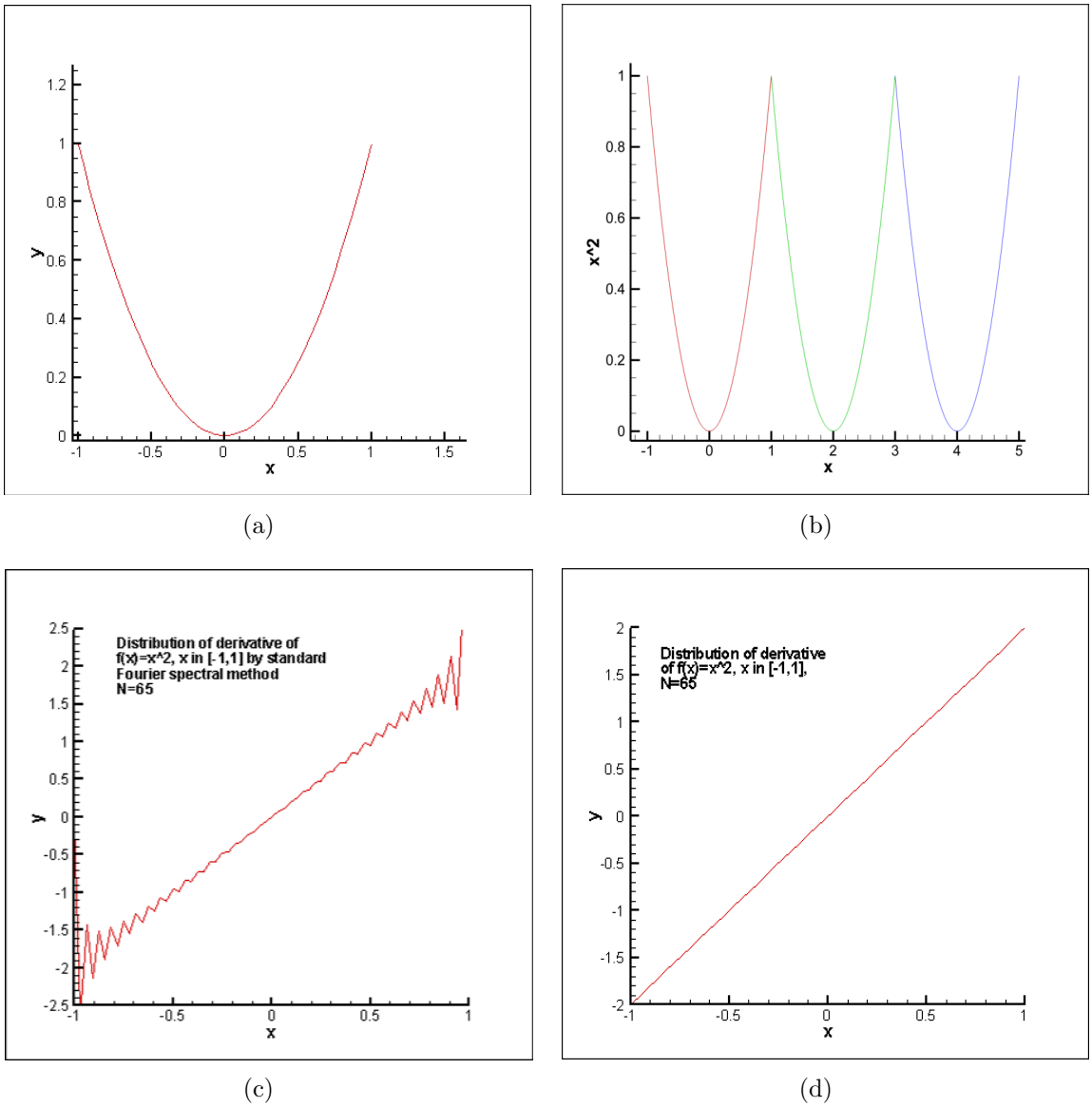

(a) (b)

(c) (d)

Figure 2.1. Sample figures (a) graphic for $y = x^2, x \in [-1, 1]$; (b) extended periodic function; (c) traditional FFT results for y'; (d) exact results for y'.

2.2.2.2 Extended smooth buffer functions

In order to solve the above problem (Gibbs phenomena), first split the original function with gaps (Figure 2.2(a)). Next use a smooth polynomial to fill the gaps as a buffer zone (Figure 2.2(b)). Note that the function is periodic and it is possible to use 8 points, 4 points from left end and 4 points from right end to construct the buffer polynomial. Assume a and b are the left and right ends of the domain of interest, one can have the following 8 points to construct the buffer polynomial (Figure 2.2(c)): $f(b-3\Delta x), f(b-2\Delta x), f(b-\Delta x), f(b)$ and $f(a), f(a+\Delta x), f(a+2\Delta x), f(a+3\Delta x)$, hence, $f(b+\delta) = f(a), f(b+\delta+\Delta x) = f(a+\Delta x), f(b+\delta+2\Delta x) = f(a+2\Delta x), f(b+\delta+3\Delta x) = f(a+3\Delta x)$, according to the periodic boundary condition. Here, δ is the length of the buffer zone. The buffer polynomial then can be written as

$$P(x) = a_0 + a_1 x + a_2 x^2 + a_3 x^3 + a_4 x^4 + a_5 x^5 + a_6 x^6 + a_7 x^7,$$

where, $a_0 - a_7$ can be determined by the given 8 points. Apparently, the buffer polynomial is determined by left and right ending 8 points and the length of δ which determines the number of buffer points. Here we use $\delta = 25\% * (b - a)$. Actually, one obtains a new function as shown in Figure 2.2(d), which is periodic both value and 1st to 7th order derivatives. The extended function with buffer is very easy for applying FFT to find the interpolation and the derivatives.

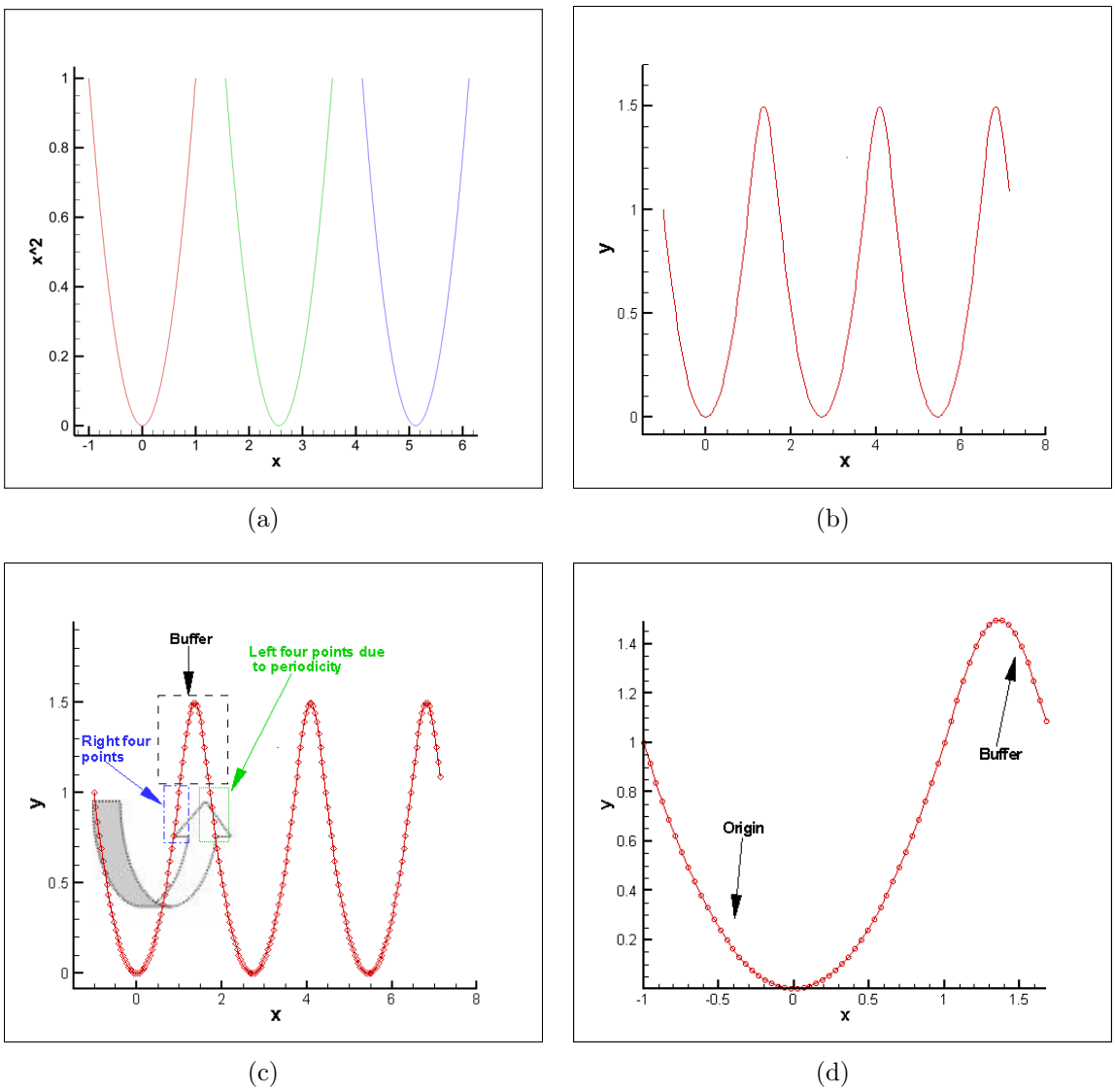

(a) (b)

(c) (d)

Figure 2.2. Buffer procedure (a) split periodic function; (b) buffered periodic function; (c) buffer polynomial construction; (d) new extended function.

The idea to construct an extended periodic function with high order polynomial as a buffer zone is the key of this BFSM method. Of course, the cost will be increased by 25% and the derivative obtained in buffer zone is non-physical and will be abandoned. However, the resolution will be much higher in comparison with reg-

ular finite difference for derivatives. Note here that the penalty of 25% is reasonable and meets the needs of most of the problems, and the using of 4 points at each end of the domain just keeps high order of accuracy, but these numbers can vary according to one's needs and the optimization could be case-related. However, the penalty of 25% is reasonable.

In the case that a function is not periodic with boundary values, serious oscillations (Gibbs phenomena) may still exist with the derivativ even we use the buffered domain and apply FFT, and the results is not acceptable. Therefore, we still need to do some recoverable modification of the boundary conditions first, that is called "normalization".

2.2.2.3 Normalization of the original function

In order to normalize the original function, we first shift the function up so that the values at the two ends of the function are positive. Note that shifting up has no affect on the derivative of the original function, since $(f+c)' = f'$. Second, we divide the function by a linear function $g(x)$, which links the two end points of the new function by a straight line, i.e., $F(x) = (f(x)+c)/g(x)$. Here, we use linear function because it is easy to be constructed and the derivative of a linear function is simple. By this procedure, the new function will be periodic with the function values on the boundary. The last step is to add a buffer domain (see section 2.2.2.2) to make the two ends of the function periodic not only the function boundary values but also the first, second, or even higher order derivatives. After doing all of these, we can use standard Fourier spectral method to get the derivative for the new extended function $F(x)$, which is periodic with function, first, second, and higher order derivatives. Then we can cut the added buffer part, and recover the derivative of the original function.

For FFT, we have to set up grids with point number to be 2^N and we use $1/4$ points of the whole number as the buffer. For example, if we set the number of all points to be 65 (with the right end point of the domain), the physical domain $[a, b]$ occupies 48 points, and the number of buffer points is 16. One can change this if necessary. Note that the second step, normalization, is also important since the large difference between two end point values will cause serious oscillations which are not acceptable, and it cannot be removed even more points are used to do the periodic interpolation.

The following is an example to introduce our method. The function we choose here is $f(x) = x^3, x \in [-1, 1]$, which has large difference between two end points.

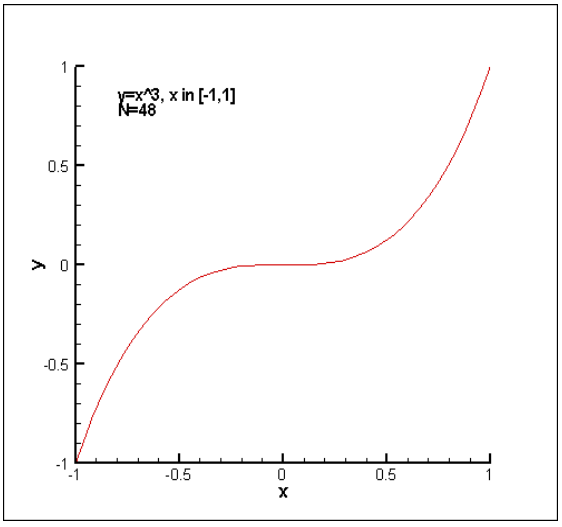

Figure 2.3. Example function $f(x) = x^3$.

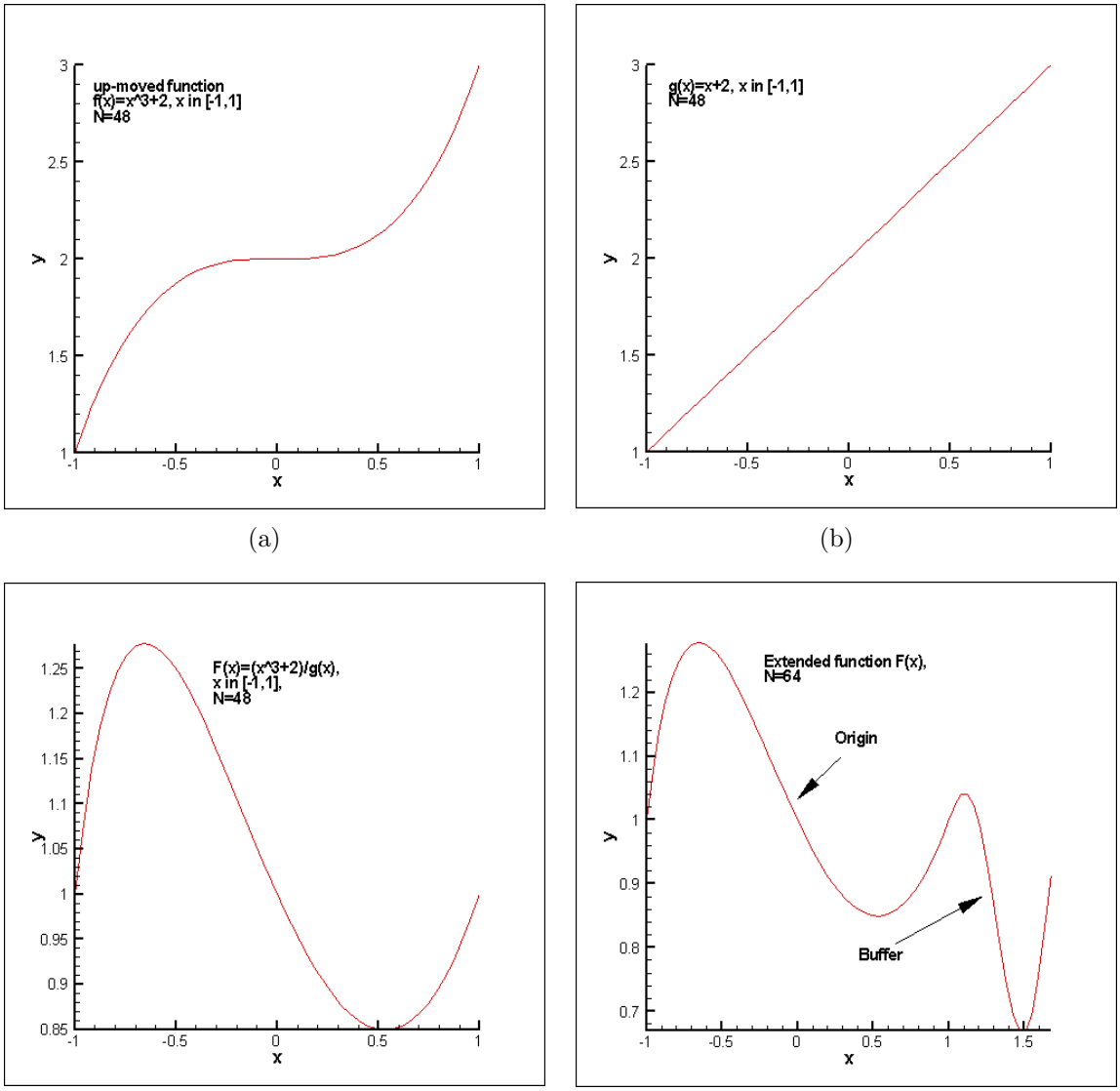

(a) (b)

(c) (d)

Figure 2.4. Example of steps (a) up-moved function $f(x) + c$; (b) linear function $g(x)$; (c) normalized function $F(x) = (f(x) + c)/g(x)$; (d) extended function with a polynomial buffer zone.

2.2.2.4 The chart of BFSM

The whole procedure can be described by the following chart:

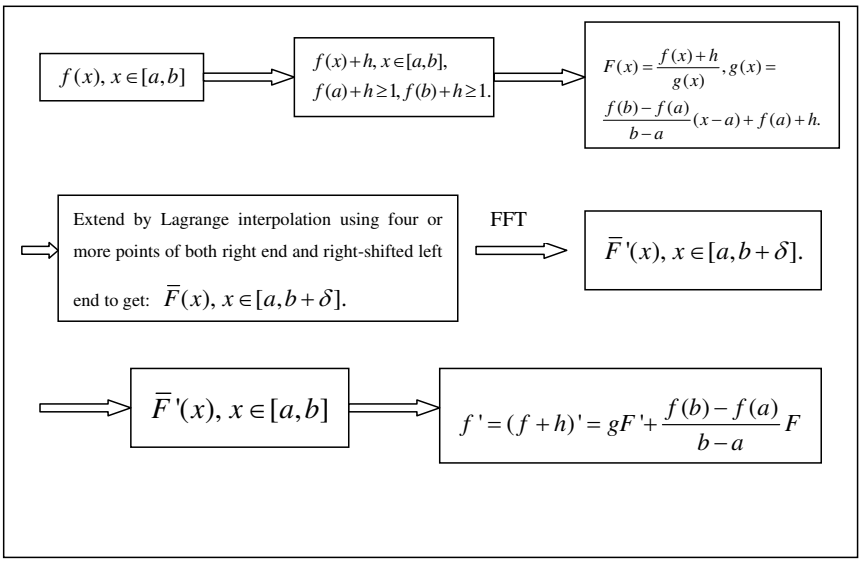

Figure 2.5. The sketch of buffered Fourier spectral method (BFSM).

2.3 Computational Results by BFSM

2.3.1 Numerical Derivative

2.3.1.1 Basic point of view on the new scheme development

Let us take an example, the 3-D time dependent Navier-Stokes equations in a general curvilinear coordinate can be written as

$$\frac{1}{J}\frac{\partial Q}{\partial t} + \frac{\partial (E - E_v)}{\partial \xi} + \frac{\partial (F - F_v)}{\partial \eta} + \frac{\partial (F - F_v)}{\partial \zeta} = 0, \tag{4.1}$$

For 1-D conservation law, it will be

$$\frac{\partial Q}{\partial t} + \frac{\partial E}{\partial \xi} = 0. \tag{4.2}$$

The critical issue for high order CFD is to find an accurate approximation of derivatives for a given discrete data set. The computer does not know any physical process but accepts a discrete data set as the input. The output is derivatives which are also a discrete data set. Therefore, it is critical to develop a high order scheme to achieve accurate derivative for a discrete data set.

2.3.1.2 BFSM for numerical derivatives

The numerical derivatives approximated by BFSM are very accurate (see Figures 2.6-2.11). Following are several non-periodic functions we tested. One can see that the main error only appears on the boundary points, which are caused by the Lagrange interpolation of the function at the buffer points. However, they are located outside the domain $[a, b]$. And we can see these errors do not propagate into the domain $[a, b]$.

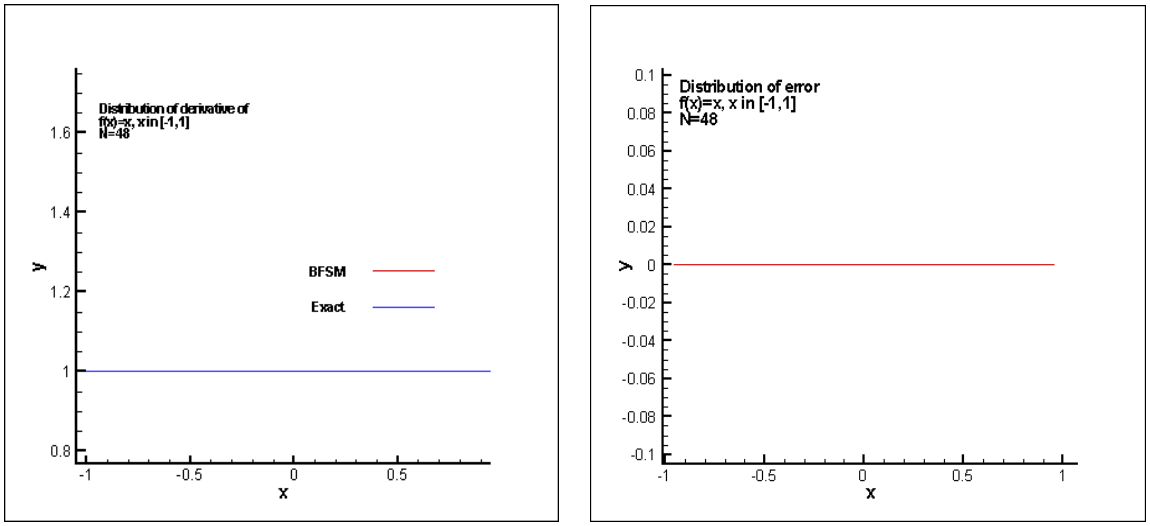

(a) (b)

Figure 2.6. $f(x) = x, x \in [-1, 1]$ (a) distribution of derivative of the function; (b) error by using BFSM.

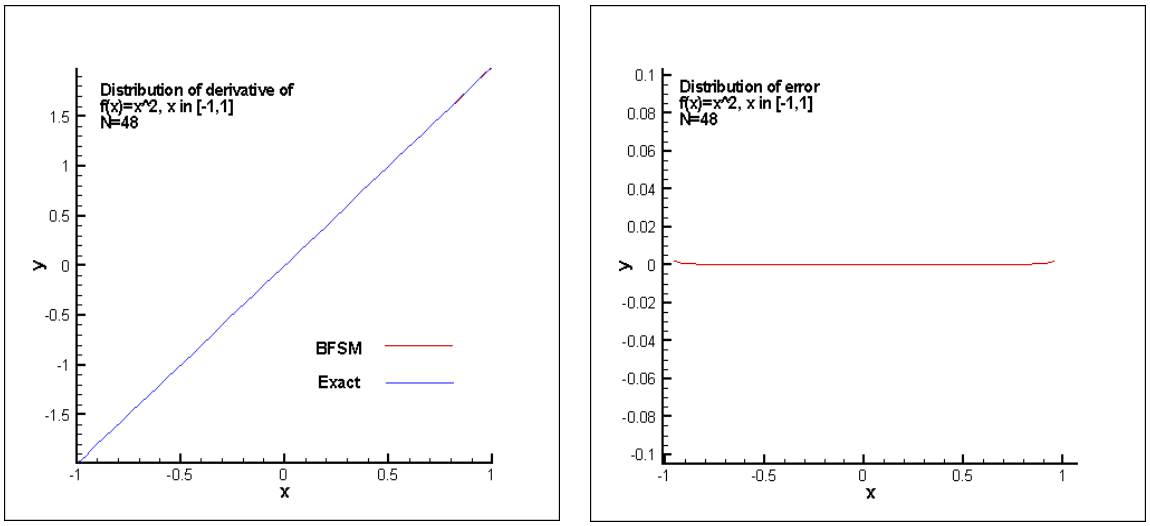

(a) (b)

Figure 2.7. $f(x) = x^2, x \in [-1, 1]$ (a) distribution of derivative of the function; (b) error by using BFSM.

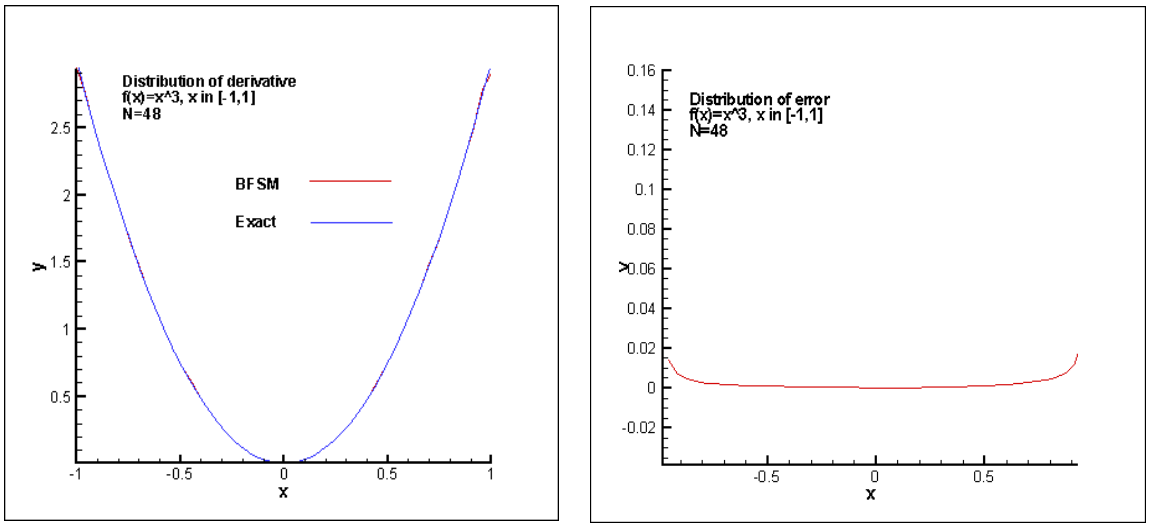

(a) (b)

Figure 2.8. $f(x) = x^3, x \in [-1, 1]$ (a) distribution of derivative of the function; (b) error by using BFSM.

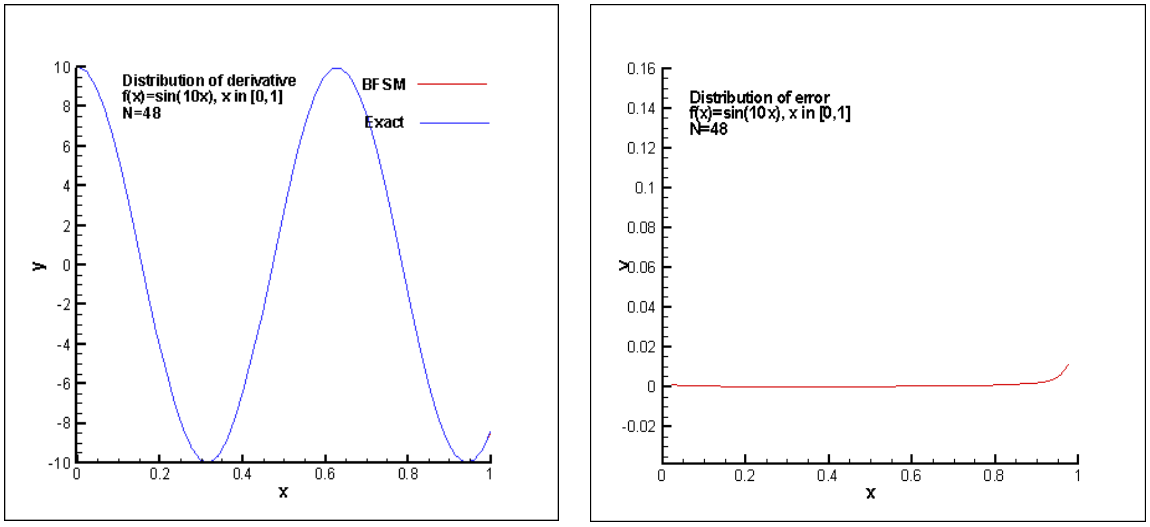

(a) (b)

Figure 2.9. $f(x) = sin(10x), x \in [0, 1]$ (a) distribution of derivative of the function; (b) error by using BFSM.

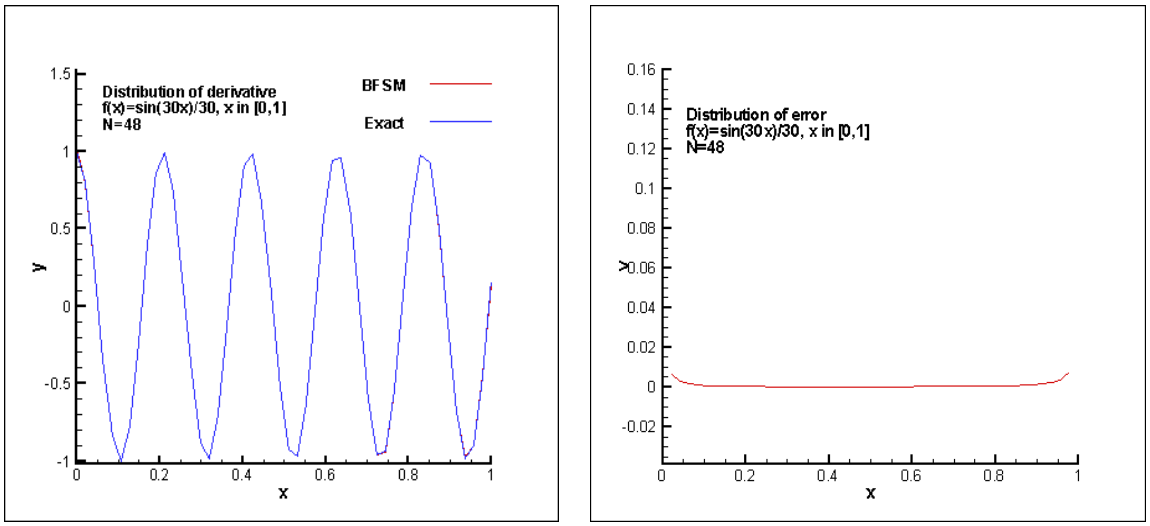

(a) (b)

Figure 2.10. $f(x) = \frac{1}{30}sin(30x), x \in [0, 1]$ (a) distribution of derivative of the function; (b) error by using BFSM.

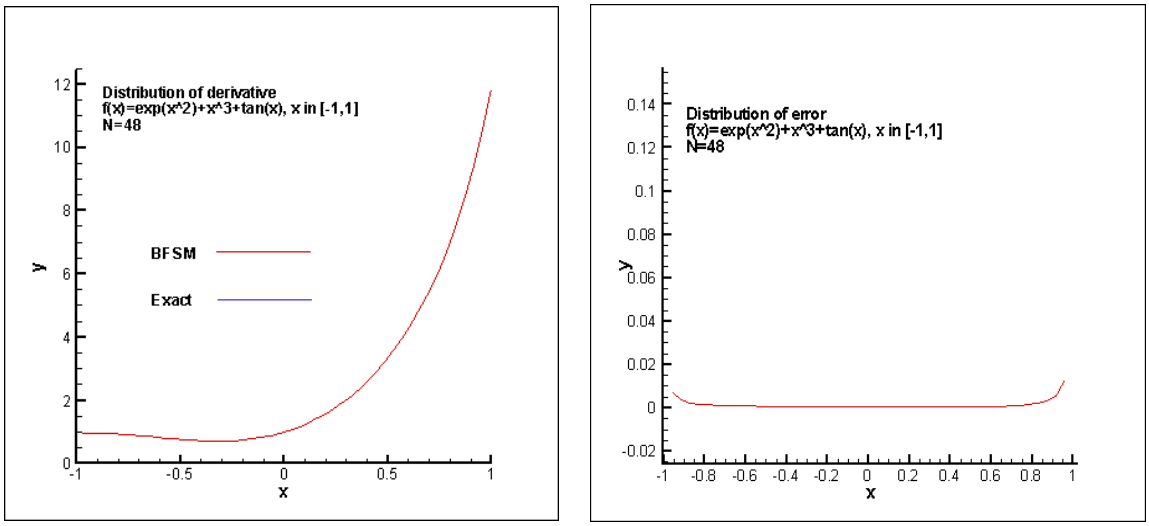

(a) (b)

Figure 2.11. $f(x) = e^{x^2} + x^3 + tan(x), x \in [-1, 1]$ (a) distribution of derivative of the function; (b) error by using BFSM.

2.3.1.3 Comparison between our BFSM and the standard spectral method

The following figures give us a picture that accurate derivatives can be obtained by applying our new method for those functions which are non-periodic (see Figures 2.12 and Figures 2.14 - 2.15). For standard Fourier spectral method, the approximation of derivatives contains a lot of oscillations, even for the function which is periodic on the boundary, such as $f(x) = x^2, x \in [-1, 1]$ (see Figure 2.12). For the functions which are non-periodic on the boundary, the standard Fourier spectral approximation of the derivatives are very oscillatory and cannot be accepted (see Figure 2.15). Note that our comparisons use different grids here for two different methods because for our new scheme we discard 25% of 64 points, but we do not need to cut 25% for the standard method. Since the grids used for standard Fourier spectral method is finer, the comparison is acceptable.

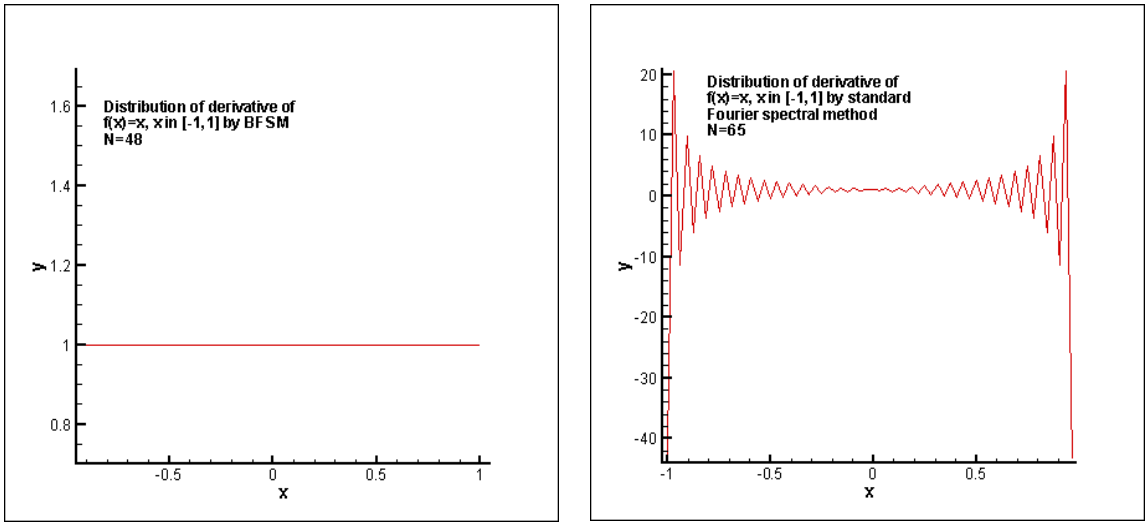

(a) (b)

Figure 2.12. Comparison between two methods for derivatives of $f(x) = x, x \in [-1, 1]$ (a) BFSM; (b) standard spectral method.

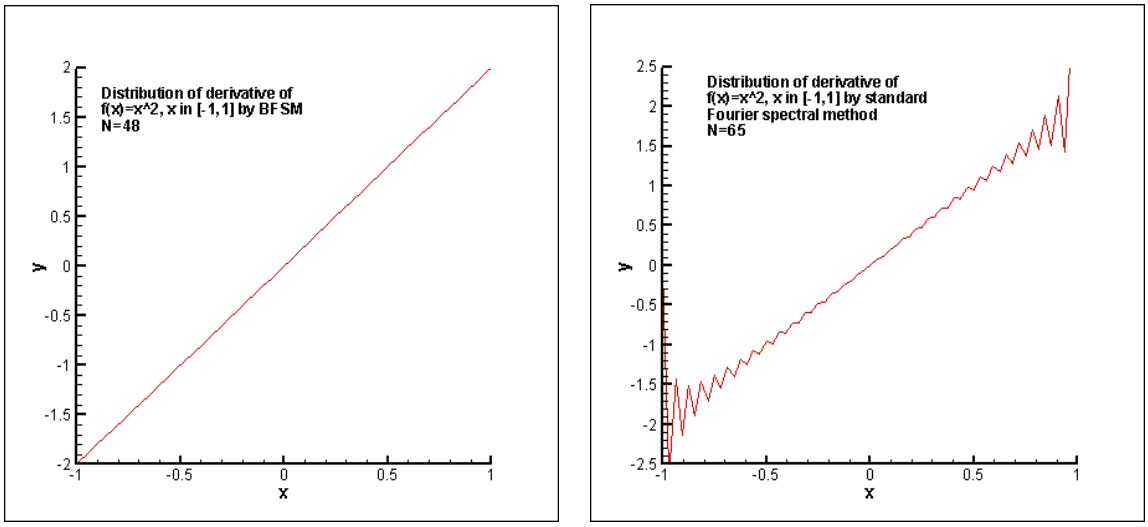

(a) (b)

Figure 2.13. Comparison between two methods for derivatives of $f(x) = x^2, x \in [-1, 1]$ (a) BFSM; (b) standard spectral method.

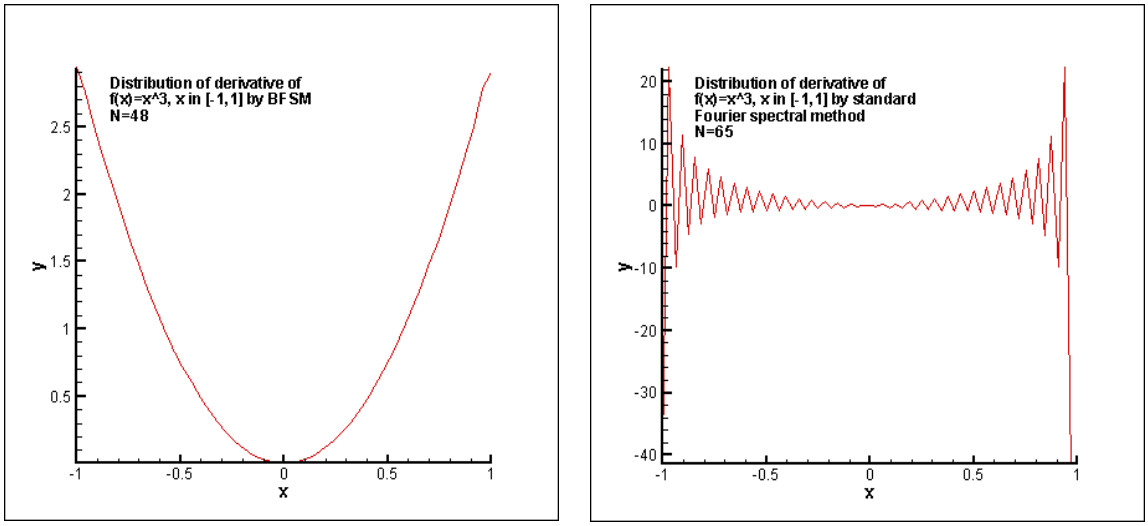

(a) (b)

Figure 2.14. Comparison between two methods for derivatives of $f(x) = x^3, x \in [-1, 1]$ (a) BFSM; (b) standard spectral method.

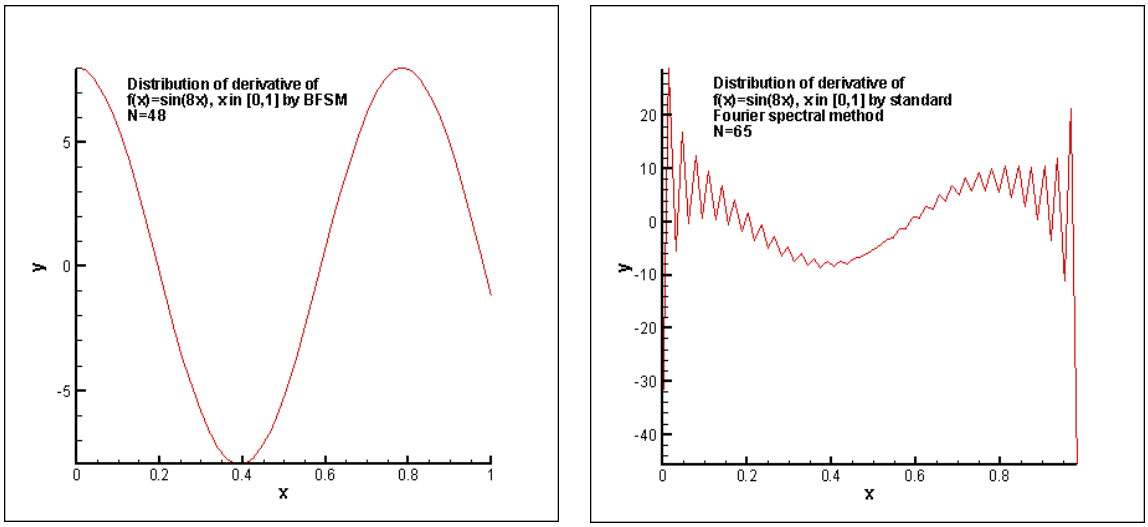

(a) (b)

Figure 2.15. Comparison between two methods for derivatives of $f(x) = sin(8x), x \in [0, 1]$ (a) BFSM; (b) standard spectral method.

2.3.1.4 Comparison between BFSM and the 2nd order central difference method

In the following figures, we compare our new method with the central finite difference scheme. We try to approximate the derivative of $f(x) = sin(8x)/8, x \in [0, 6]$ and $f(x) = sin(20x)/20, x \in [0, 6]$. These are high frequency waves and we want to compare the capability for high resolution between BFSM and the central finite difference method. From Figure 2.16, we see that the central difference does not work well and has visible large errors even for $f(x) = sin(8x)/8, x \in [0, 6]$, but Buffered Fourier Spectral Method works very well except for the boundary points due to the artificial interpolation polynomial. For the higher frequency function $f(x) = sin(20x)/20, x \in [0, 6]$, the central difference loses accuracy and the results are completely unacceptable, but our new method works very well. From these two graphs, we see that although we use only 48 points in [0, 6], our results are nearly the same as the exact solution (the blue one and the black one overlap each other), which means our new method has high order accuracy and high resolution. But the results approximated by central difference are not acceptable and even worse for higher frequencies (Figure 2.17). This clearly shows that BFSM has much higher resolution than standard central finite difference schemes.

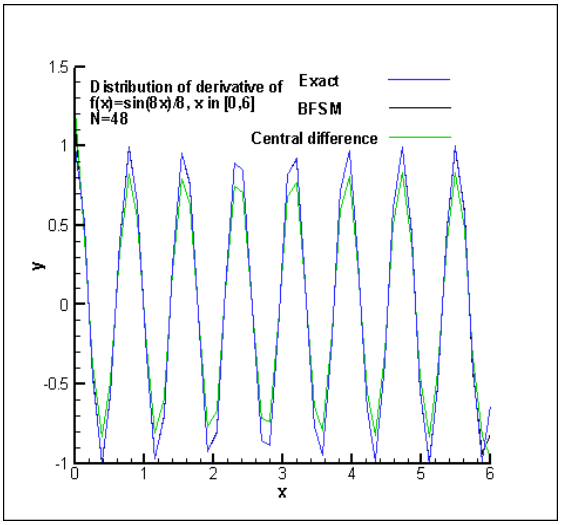

Figure 2.16. Comparison between BFSM and central difference for derivatives, $N = 48$, $f(x) = sin(8x)/8, x \in [0, 6]$.

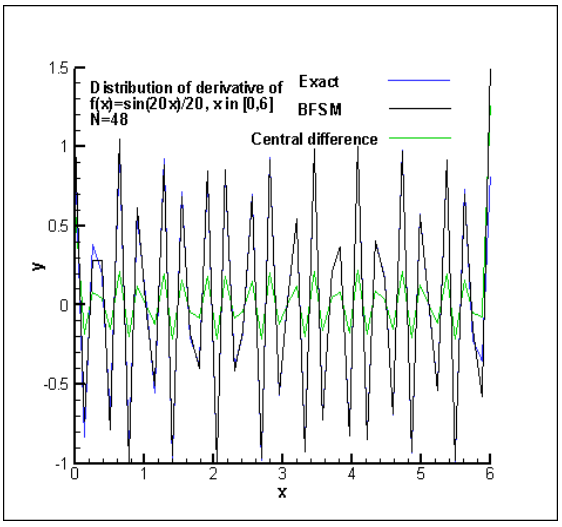

Figure 2.17. Comparison between BFSM and central difference for derivatives, $N = 48$, $f(x) = sin(20x)/20, x \in [0, 6]$.

2.3.2 Wave Equation

For a wave equation $u_t + cu_x = 0, u(0,x) = f(x)$, we solve the equation under different initial boundary conditions and different grids. The exact solution is $u(t,x) = f(x-ct)$. In addition, we perform comparisons between our new method and second order central difference scheme. For time marching, both methods use the 4-th order Runge-Kutta method and both central and BFSM methods are conditionally stable. We use a Courant number 0.5 for all following calculations. One should note that all boundary conditions are not periodic here. Figures 2.18 - 2.21 give us a picture that our method is of fourth order, which is determined by the interpolation on the boundary. And these figures also show us that the Buffered Fourier Spectral Method can obtain high resolution. By the comparisons in Figure 2.19 and Figure 2.20, one can easily see that the 2nd-order central difference results are just simply not acceptable after some time steps, but our new method still works very well. For the initial boundary condition $f(x) = sin(20x), x \in [0,6]$, our new method still can resolve the high frequency waves and obtain nearly same results as the exact solution. On the other hand, the second order central difference scheme can work for the initial boundary condition of $f(x) = sin(x), x \in [0,1]$ with large errors, but completely fail for the initial boundary conditions of $f(x) = sin(8x), x \in [0,6]$ and $f(x) = sin(20x), x \in [0,6]$. We also tested up-winding schemes (1st order) for the boundary condition $f(x) = sin(8x), x \in [0,6]$, the results of which are not acceptable.

a). Initial condition: $f(x) = sin(x), x \in [0,1]$, $N = 96$.

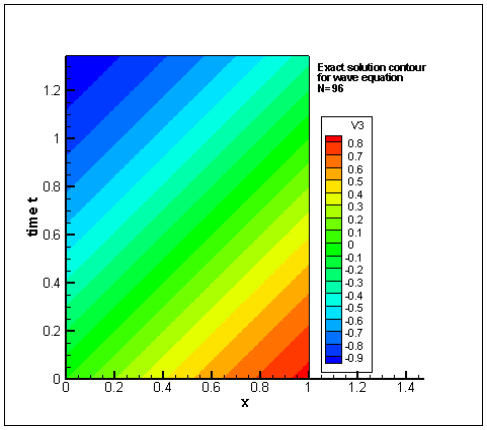

(a)

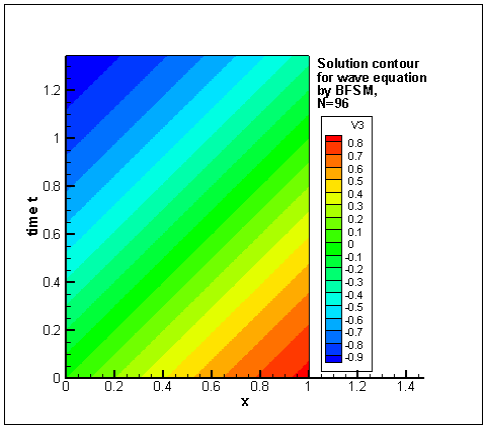

(b)

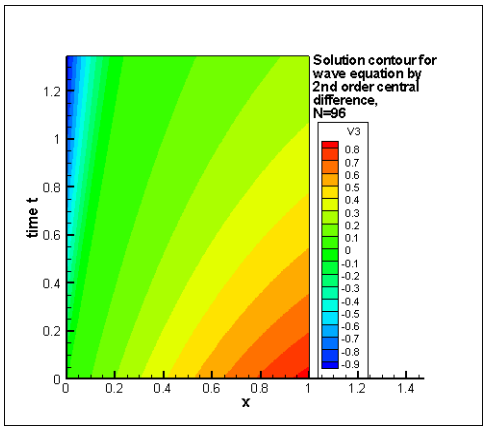

(c)

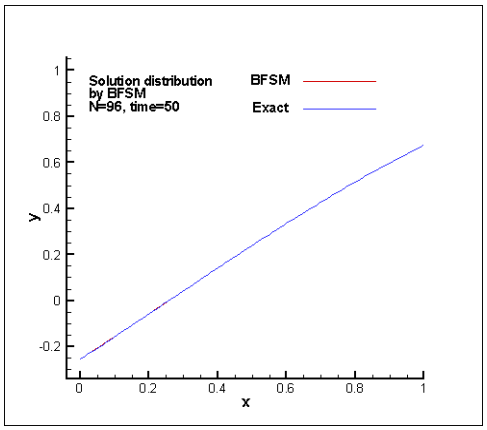

(d)

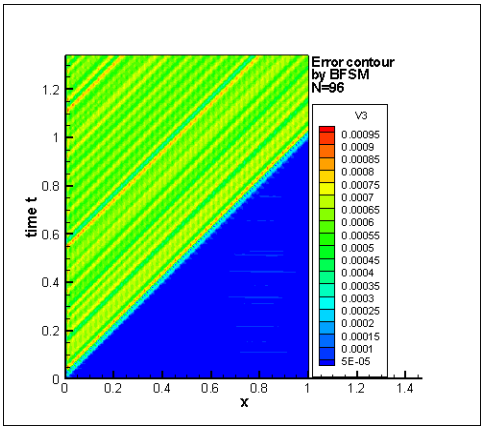

(e)

Figure 2.18. Solution of wave equation with initial condition $f(x) = sin(x), x \in [0, 1]$, $N = 96$ (a) exact solution; (b) BFSM; (c) central difference; (d) distribution of u at $t = 50$ by BFSM; (e) error contour by BFSM.

b). Initial condition: $f(x) = sin(8x), x \in [0, 6]$, $N = 48$.

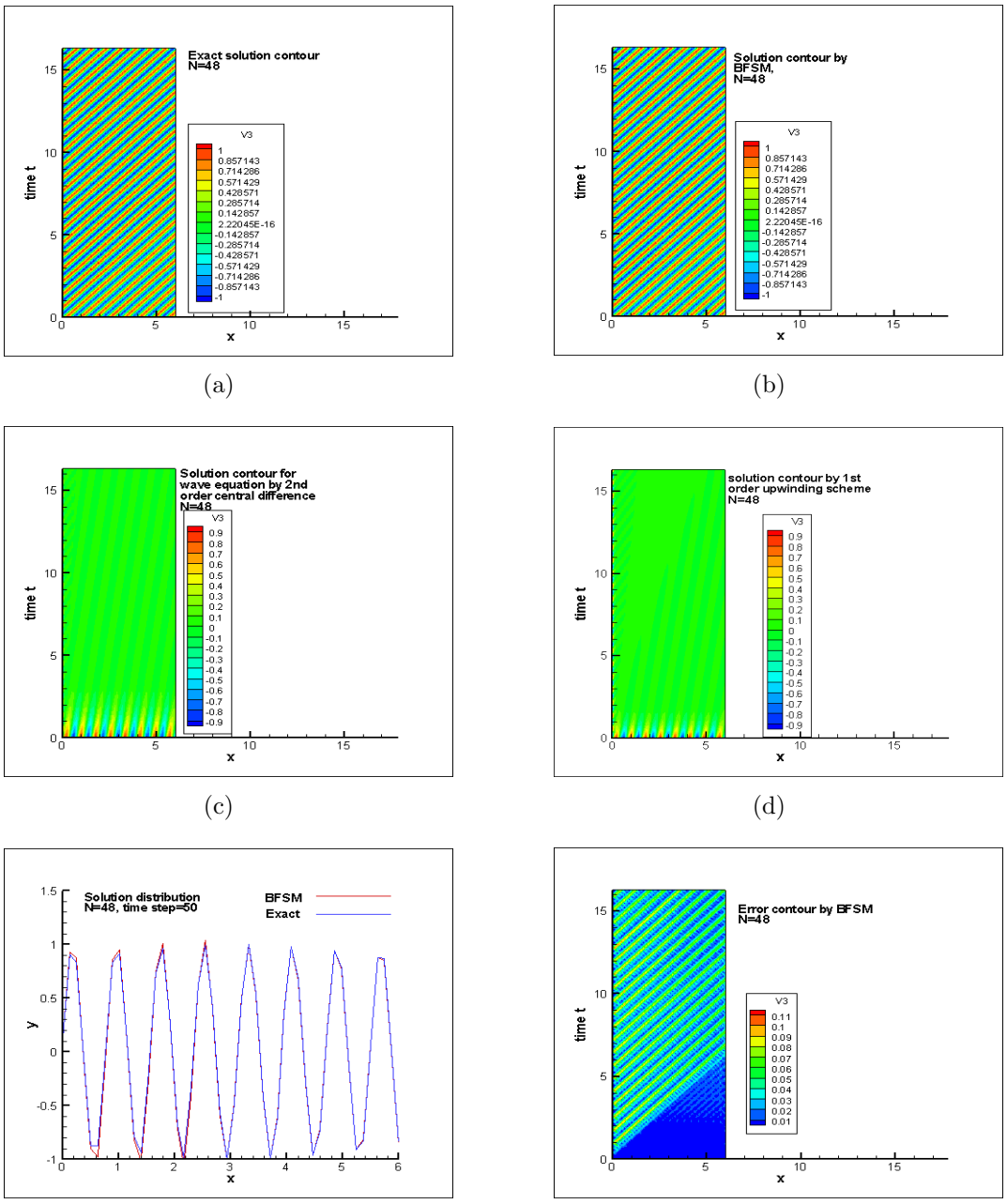

(a) (b) (c) (d) (e) (f)

Figure 2.19. Solution of wave equation with initial condition $f(x) = sin(8x), x \in [0, 6]$, $N = 48$ (a) exact solution; (b) BFSM; (c) central difference; (d) 1st order upwinding; (e) distribution of u at $t = 50$ by BFSM; (f) error contour by BFSM.

c). Initial condition: $f(x) = sin(8x), x \in [0, 6]$, $N = 96$.

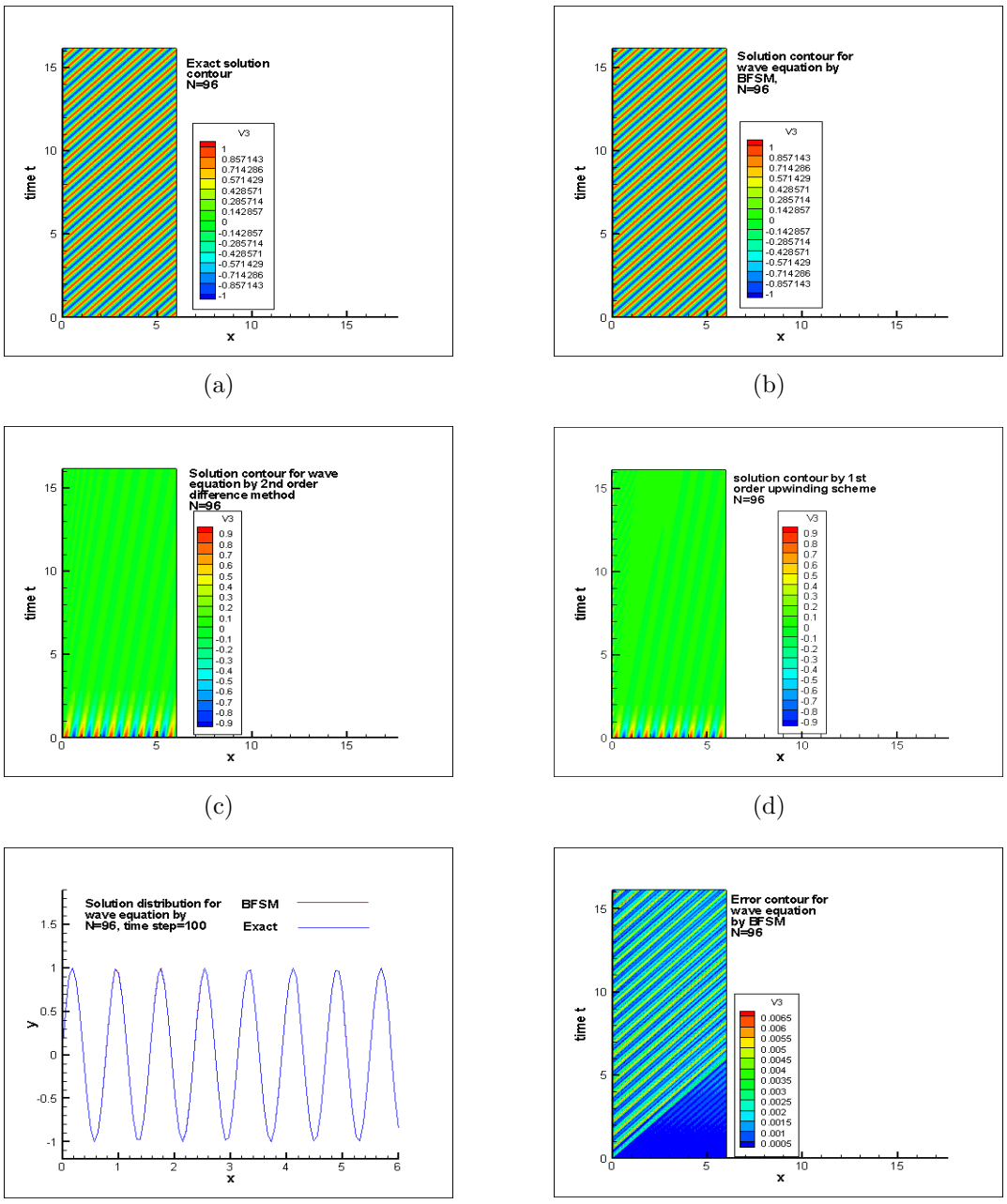

(a) (b) (c) (d) (e) (f)

Figure 2.20. Solution of wave equation with initial condition $f(x) = sin(8x), x \in [0, 6]$, $N = 96$ (a) exact solution; (b) BFSM; (c) central difference; (d) 1st order upwinding; (e) distribution of u at $t = 100$ by BFSM; (f) error contour by BFSM.

d). Initial condition: $f(x) = sin(20x), x \in [0, 6]$, $N = 96$.

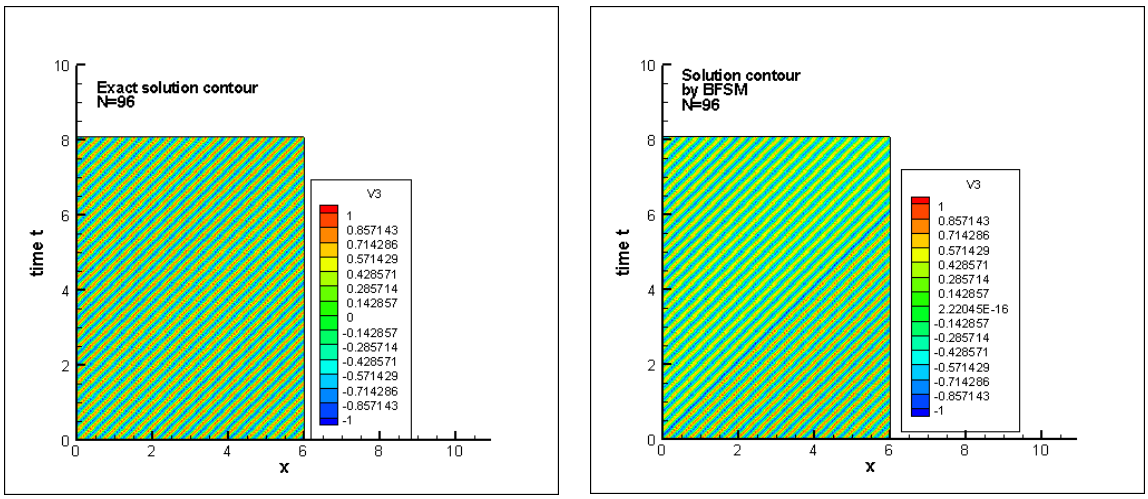

(a) (b)

Figure 2.21. Solution of wave equation with initial condition $f(x) = sin(20x), x \in [0, 6]$, $N = 96$ (a) exact solution; (b) BFSM.

2.3.3 Poisson's Equation

2.3.3.1 Governing equations

Poisson's equation is of elliptic type with broad utility in electrostatics, mechanical engineering and theoretical physics, and it is commonly used to model diffusion. The definition of Poisson's equation is as following,

$$\Delta\phi = f,$$

where Δ is the Laplace operator, and ϕ and f are real or complex functions.

In three-dimensional Cartesian coordinates, it takes the form

$$(\frac{\partial^2}{\partial x^2} + \frac{\partial^2}{\partial y^2} + \frac{\partial^2}{\partial z^2} +)\phi(x, y, z) = f(x, y, z).$$

For $f = 0$, the equation reduces to Laplace's equation.

2.3.3.2 Numerical results

We now use our new method for Poisson's equation with non-periodic boundary conditions. The problem is defined as following,

$$\begin{cases} \Delta u = 0, \quad (x, y) \in [0, 1] \times [0, 1]; \\ u(x, 0) = e^x \sin(x); \ u(0, y) = e^{-y} \sin(y); \\ u(1, y) = e^{1-y} \sin(1 + y); \ u(x, 1) = e^{x-1} \sin(x + 1). \end{cases}$$

The exact solution is $u(x, y) = e^{x-y} sin(x + y), (x, y) \in [0, 1] \times [0, 1]$. We solve the equation by using following equation for iteration,

$$u_{t+1} = u_t + \Delta t(u_{xx} + u_{yy}).$$

The convergence tolerance was set to be $|u_{t+1} - u_t| \leq 10^{-12}$, and we use 6 points at each end of the boundary to do the interpolation.

The following figures are our results.

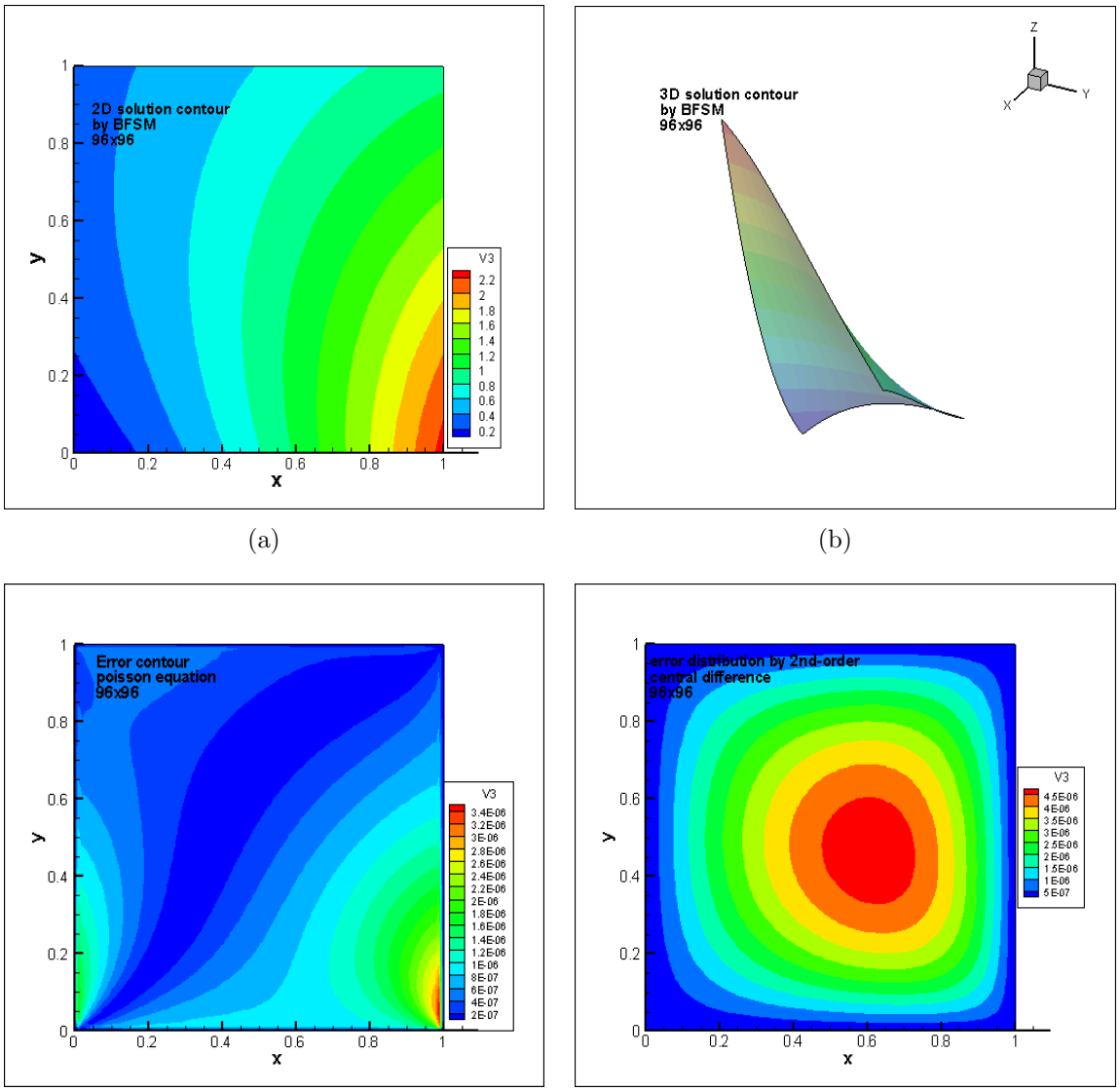

(a) (b)

(c) (d)

Figure 2.22. Solution and error contour, grids: 96×96 (a) 2D solution contour; (b) 3D solution contour; (c) error contour by BFSM; (d) error contour by 2nd order central difference.

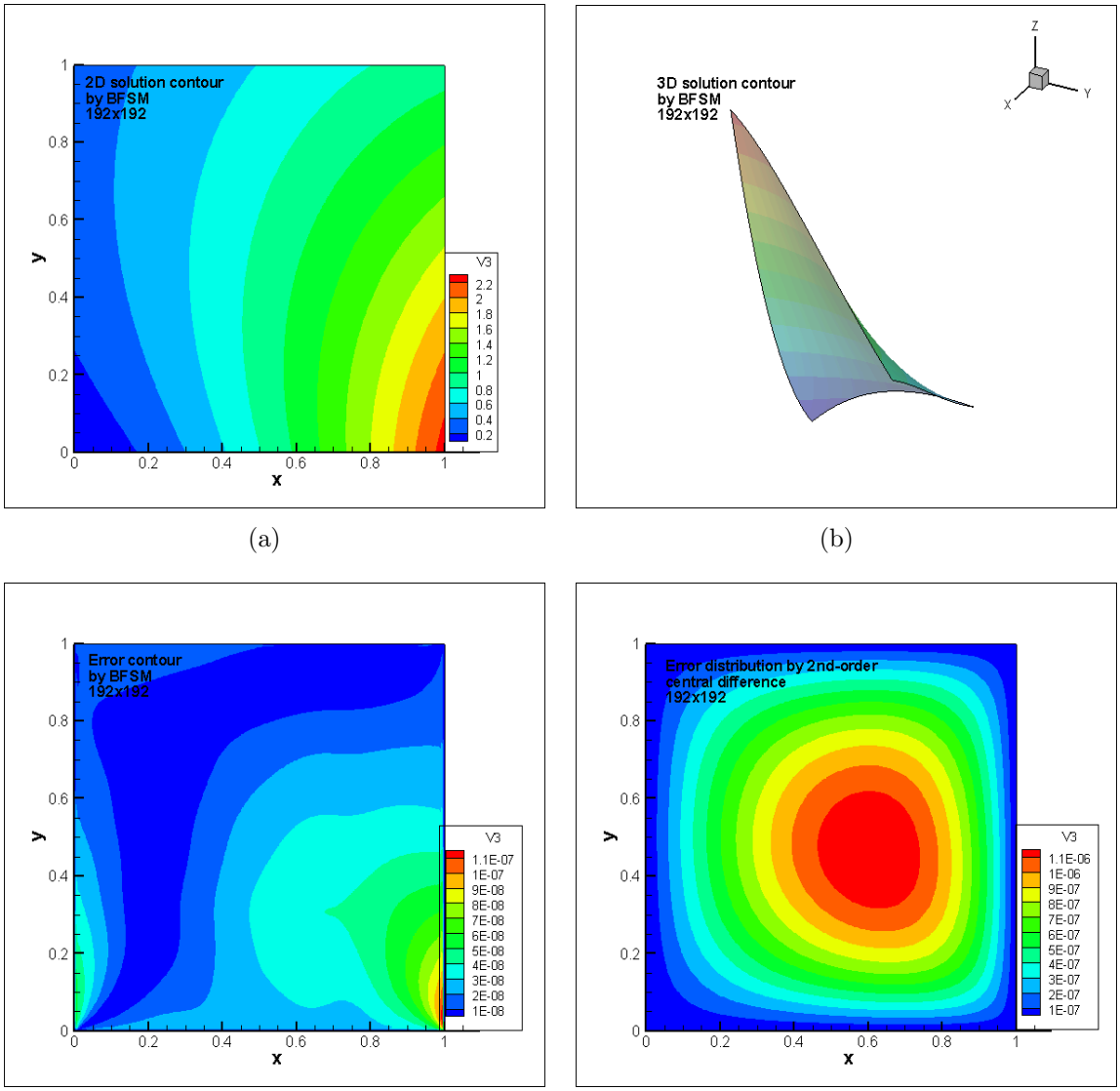

(a) (b)

(c) (d)

Figure 2.23. Solution and error contour, grids: 192×192 (a) 2D solution contour; (b) 3D solution contour; (c) error contour by BFSM; (d) error contour by 2nd order central difference.

Table 2.1. Maximum error comparison

GRids	BFSM	2nd-order central difference
96×96	$3.5847E-6$	$4.8255E-6$
192×192	$1.1874E-7$	$1.1971E-6$

From the above table, we can see the order of accuracy for BFSM is 5, which is partially determined by the boundary treatment. However, the 2nd order central difference has only order 2 of accuracy. From those Figures, we can get a picture that for BFSM, the largest error primarily appears on the boundary, and is related to the function value differences between two end points, while the error for central difference occupies most of the middle area. From the error figures, we can see that near the bottom of the left and right sides, the errors are larger than other area. This is because the differences of function (or solution) values between those two end points in the x direction is large. However, near both top and bottom sides, the errors are not large since the differences between these two end points in y direction are smaller. In the interior area, the BFSM solution is very accurate, almost same as the exact solution. In general, we say that the large errors happen only near the boundary which is caused by the manually extending the function and doing the polynomial interpolation. However, this is acceptable because of the non-periodicity of the function.

2.3.4 2D Lid Driven Cavity Flow

2.3.4.1 Governing equations

For 2-D lid driven cavity flow, the system in stream function and vorticity function is

$$\begin{cases} \dfrac{\partial^2\Psi}{\partial x^2} + \dfrac{\partial^2\Psi}{\partial y^2} = -\omega; \\ \dfrac{1}{Re}(\dfrac{\partial^2\omega}{\partial x^2} + \dfrac{\partial^2\omega}{\partial y^2}) = \dfrac{\partial\Psi}{\partial y}\dfrac{\partial\omega}{\partial x} - \dfrac{\partial\Psi}{\partial x}\dfrac{\partial\omega}{\partial y} \\ \qquad\qquad\qquad\qquad = u\dfrac{\partial\omega}{\partial x} + v\dfrac{\partial\omega}{\partial y}\ , \end{cases}$$

where $u(x,y) = \dfrac{\partial\Psi}{\partial y}, v(x,y) = -\dfrac{\partial\Psi}{\partial x}, \omega = \dfrac{\partial v}{\partial x} - \dfrac{\partial u}{\partial y}$. In our computation, the domain is chosen as $[0,1] \times [0,1]$, and the boundary conditions are $u = 0$ on the wall and bottom except on the lid at the top, and $v = 0$ for all boundaries. The Reynolds number Re here we choose as 100 and 400, respectively. To use our numerical scheme, we modify the equations to be the following time related equations,

$$\begin{cases} \dfrac{\partial\Psi}{\partial t} = \dfrac{\partial^2\Psi}{\partial x^2} + \dfrac{\partial^2\Psi}{\partial y^2} + \omega; \\ \dfrac{\partial\omega}{\partial t} = \dfrac{1}{Re}(\dfrac{\partial^2\omega}{\partial x^2} + \dfrac{\partial^2\omega}{\partial y^2}) - \dfrac{\partial\Psi}{\partial y}\dfrac{\partial\omega}{\partial x} + \dfrac{\partial\Psi}{\partial x}\dfrac{\partial\omega}{\partial y} \\ \qquad = \dfrac{1}{Re}(\dfrac{\partial^2\omega}{\partial x^2} + \dfrac{\partial^2\omega}{\partial y^2}) - u\dfrac{\partial\omega}{\partial x} - v\dfrac{\partial\omega}{\partial y}\ , \end{cases}$$

and then apply forth order Runge-Kutta time marching method to get the results.

2.3.4.2 Numerical results

Numerical results are calculated under two different Reynolds numbers, 100 and 400, respectively. And both of the calculations use the grids 47×47.

(1). $Re = 100$, grids: 47×47.

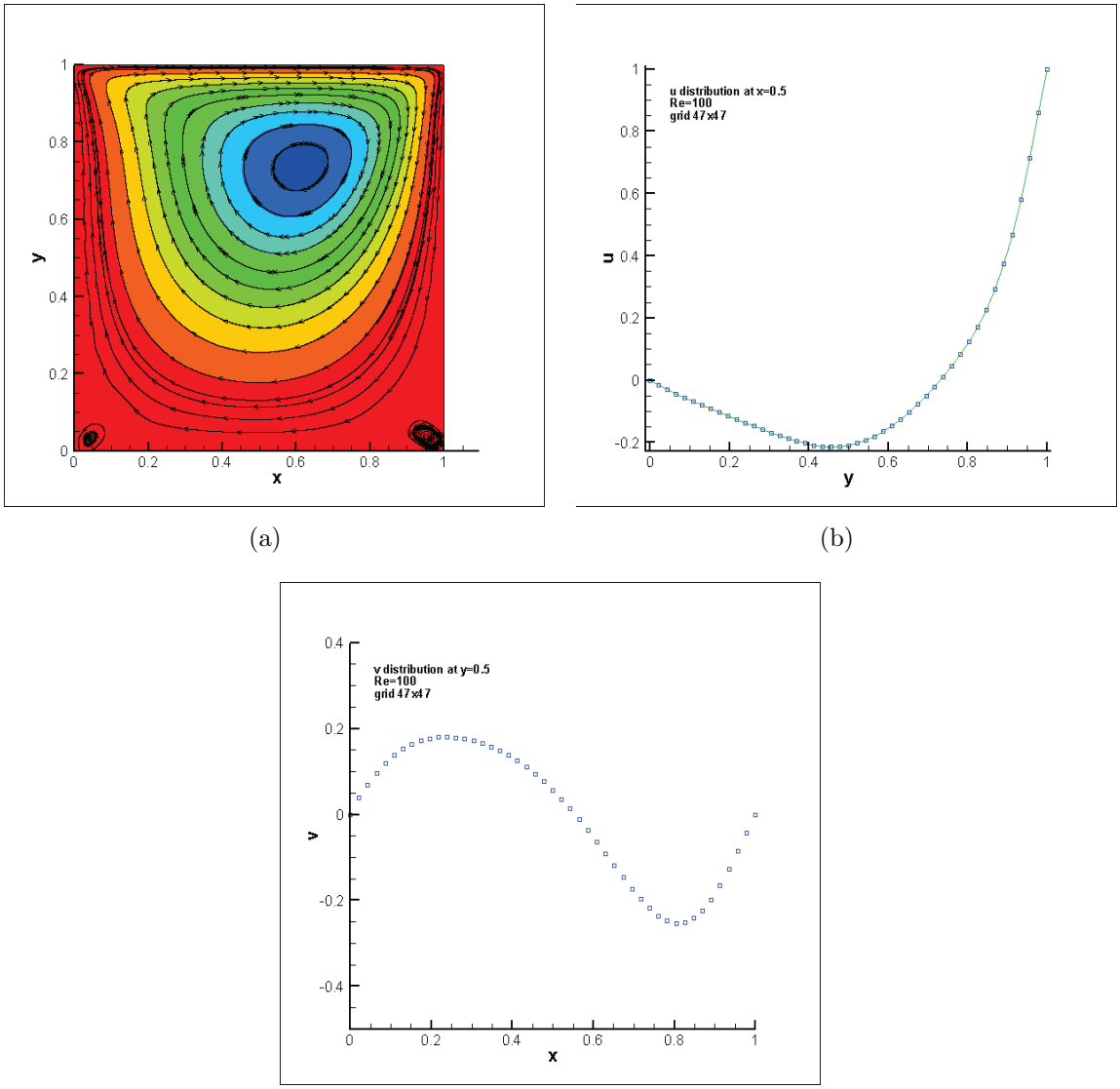

(a) (b)

(c)

Figure 2.24. Solution with $Re = 100$ (a) stream contour and stream line; (b) u distribution at $x = 0.5$; (c) v distribution at $y = 0.5$.

Table 2.2. Properties of the center of primary vortex, $Re = 100$.

Primary votex	Our results (47×47)	Ghia (129×129)
center	(0.619565,0.728261)	(0.6172,0.7344)
ω	3.16872	3.16646
Ψ	-0.103491	-0.103423

(2). $Re = 400$, grids: 47×47.

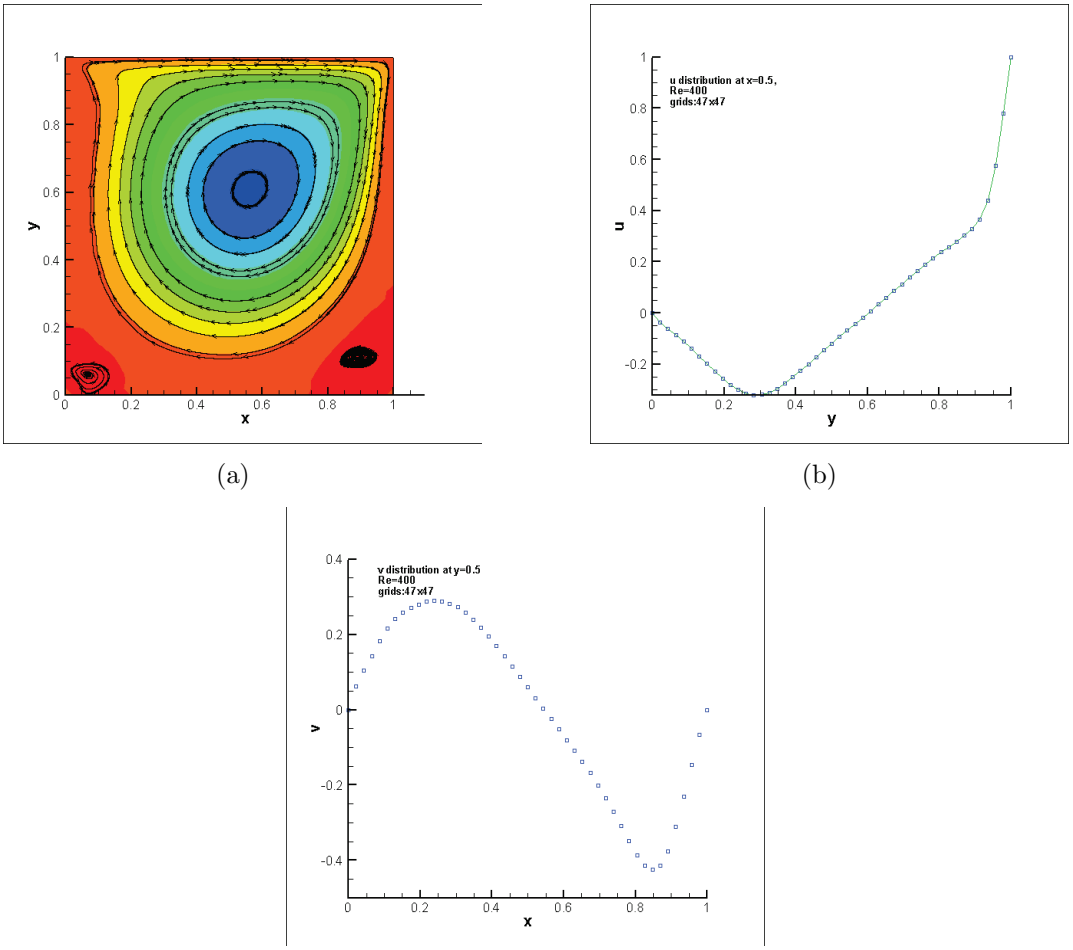

(a) (b)

(c)

Figure 2.25. Solution with $Re = 400$ (a) stream contour and stream line; (b) u distribution at x=0.5; (c) v distribution at $y = 0.5$.

Table 2.3. Properties of the center of primary vortex, $Re = 400$

Primary votex	Our results (47×47)	Ghia (257×257)
center	(0.554348,0.597826)	(0.5547,0.6055)
ω	2.33164	2.29469
Ψ	-0.111896	-0.113909

2.4 Concluding Remarks

1. Using smooth buffer and normalization, the non-periodic smooth function can be extended to a periodic function which is smooth in functions and derivatives, and therefore the standard Fourier spectral method can be used to such a new buffered function.

2. The Buffered Fourier Spectral Method (BFSM) can get very accurate numerical derivatives for non-periodic functions. Large errors only happen near the boundary because of the non-periodicity of the function or solution and polynomial interpolation.

3. The Buffered Fourier Spectral Method keeps high resolution and high order accuracy for smooth PDEs, and the order of accuracy is determined by the interpolation on the boundary. Non-smooth PDEs are still open for further research.

4. With some penalty over the standard FSM method, BFSM still keeps high order of accuracy and high resolution for non-periodic PDEs.

CHAPTER 3

MODIFIED WEIGHTED COMPACT SCHEME

Although BFSM can be applied to solve PDEs with non-periodic boundary condition, for shocks or large gradient, it is not feasible, this comes this chapter, Modified Weighted Compact Scheme.

3.1 Numerical Formula

The MWCS combines the WENO scheme and WCS where the mixing function relies on the weights of WCS. In the present section, a description of the three high order schemes is provided. To get started, we need to review some basic notations about Flux and Derivatives.

3.1.1 Flux and Derivative

To review the different schemes starting from a common framework, it is convenient to consider the scalar conservation equation in the one-dimensional case,

$$q_t(x,t) + F_x(u(x,t)) = 0. \tag{3.1}$$

Discretizing the domain, we define a grid (cell interfaces) as

$$a = x_{1/2} < x_{3/2} < ... < x_{N-1/2} < x_{N+1/2} = b. \tag{3.2}$$

The cell center and cell sizes are defined by

$$x_j \equiv \frac{1}{2}\left(x_{j-1/2} + x_{j+1/2}\right), \quad h_j \equiv x_{j+1/2} - x_{j-1/2}, \quad j = 1, 2, ..., N.$$

The grid described above is shown in Figure 3.1, where the dots denote cell centers, and triangles denote the cell interfaces (3.2).

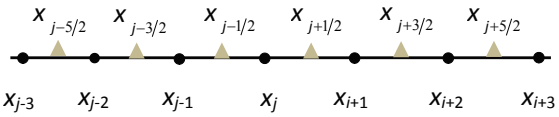

Figure 3.1. Grid for the one-dimensional case.

A semi-discrete conservative form of (3.1) reads as

$$\frac{\mathrm{d}\, q_j}{\mathrm{d}\, t} = -\frac{1}{h_j}\left(\hat{F}_{j+1/2} - \hat{F}_{j-1/2}\right), \tag{3.3}$$

where $\hat{F}$ is the numerical flux associated to the original function F, defined implicitly by $F_j = F(q(x_j,t)) \equiv \int_{x_{j-1/2}}^{x_{j+1/2}} \hat{F}(\xi)\mathrm{d}\xi$. With the given implicit definition of the numerical flux $\hat{F}$, equation (3.3) constitutes as an exact expression of (3.1).

We denote H as the primitive function of $\hat{F}_\xi$, which can be calculated by

$$H_{j+1/2} = H(x_{j+1/2}) = \int_{-\infty}^{x_{j+1/2}} \hat{F}(\xi)\mathrm{d}\xi = \sum_{i=-\infty}^{j} \int_{x_{j-1/2}}^{x_{j+1/2}} \hat{F}(\xi)\mathrm{d}\xi = \sum_{I=-\infty}^{j} F_i h_i. \tag{3.4}$$

So the primitive function H is calculated from the discrete data set of the original function F. Note that the derivative of the primitive function at the cell interfaces coincides with the numerical flux, i.e.,

$$H'_{j+1/2} = \hat{F}_{j+1/2}.$$

It is clear that

$$F_x(x_j) = F'_j = \frac{\hat{F}_{j+1/2} - \hat{F}_{j-1/2}}{h_j} = \frac{H'_{j+1/2} - H'_{j-1/2}}{h_j}. \tag{3.5}$$

In the described procedure $F \to H \to \hat{F} \to F'$ which is introduced by [4], the only approximation involved is the calculation of the derivative of the primitive function H', whereas all other calculations are exact. The intermediate step through the primitive function H is of crucial importance for the WENO and WCS schemes which is reviewed in the next a few paragraphs.

3.1.2 The 5th Order Weighted Essentially Non-Oscillatory (WENO) Scheme

For integrity, the 5th order WENO will be described as following. Considering the one dimensional hyperbolic equation

$$\frac{\partial u}{\partial t} + \frac{\partial F(u)}{\partial x} = 0. \tag{3.6}$$

The semi-discretized equation by the conservative scheme can be expressed as

$$(\frac{\partial u}{\partial t})_j = -\frac{H_{j+1/2} - H_{j-1/2}}{\Delta x}, \tag{3.7}$$

where $H_{j+1/2} = H\left(F_{j+1/2}\right)$ and for second order scheme, $H_{j+1/2} = F_{j+1/2}$.

The basic ideas of the weighted schemes like WENO are as follows,

(1). Apply basic grid stencils and difference schemes on them;

(2). Combine these schemes on different stencils and get linear weights to obtain higher order;

(3). Obtain nonlinear weights to make the scheme adaptive to discontinuity like shock waves.

Figure 3.2 shows the basic grid stencils for standard 5th order WENO scheme.

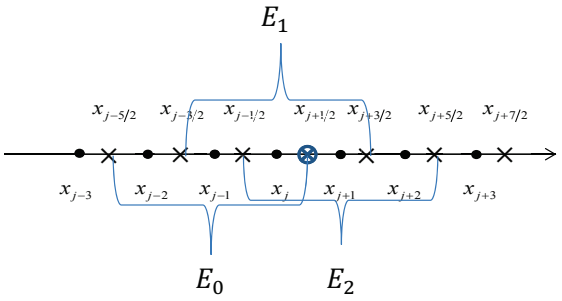

Figure 3.2. Grid for the one-dimensional case.

i.e.,

$$E_0 = \{x_{j-2}, x_{j-1}, x_j\}, E_0 = \{x_{j-1}, x_j, x_{j+1}\}, E_0 = \{x_j, x_{j+1}, x_{j+2}\}. \tag{3.8}$$

Considering the positive flux, the three upwind-biased schemes on three candidates E_0, E_1 and E_2 can be given as

$$\begin{aligned}
E_0: \quad \hat{F}^{(E_0)}_{j+1/2} &\approx \frac{1}{3}F_{j-2} - \frac{7}{6}F_{j-1} + \frac{11}{6}F_j; \\
E_1: \quad \hat{F}^{(E_1)}_{j+1/2} &\approx -\frac{1}{6}F_{j-1} + \frac{5}{6}F_j + \frac{1}{3}F_{j+1}; \\
E_2: \quad \hat{F}^{(E_2)}_{j+1/2} &\approx \frac{1}{3}F_j + \frac{5}{6}F_{j+1} - \frac{1}{6}F_{j+2}.
\end{aligned}$$

If we take the weighted average of the three low-order approximations above, with the constant optimal weights

$$C_0 = \frac{1}{10}, \qquad C_1 = \frac{6}{10}, \qquad C_2 = \frac{3}{10}, \tag{3.9}$$

then we obtain

$$\hat{F}_{j+1/2} \approx \sum_{i=0}^{2} C_i \hat{F}^{(E_i)}_{j+1/2} = \frac{1}{30}F_{j-2} - \frac{13}{60}F_{j-1} + \frac{47}{60}F_j + \frac{9}{20}F_{j+1} - \frac{1}{20}F_{j+2}.$$

Note that the constant weights in (3.9) sum up to 1 for consistency, i.e., $\sum_{i=0}^{2} C_i = 1$. After the expression of the approximation for $\hat{F}_{j-1/2} = \hat{F}_{(j-1)+1/2}$ is obtained in analogous fashion as above, we can calculate the discrete approximation to the derivative of the original function as (see the semi-discrete equation (3.7))

$$\begin{aligned}
F'_j &= \frac{\hat{F}_{j+1/2} - \hat{F}_{j-1/2}}{h_j} \\
&\approx \frac{-\frac{1}{30}F_{j-3} + \frac{1}{4}F_{j-2} - F_{j-1} + \frac{1}{3}F_j + \frac{1}{2}F_{j+1} - \frac{1}{20}F_{j+2}}{h_j}.
\end{aligned} \tag{3.10}$$

It is easy to verify by a Taylor series expansion that equation (3.10) is a 5th order approximation to the discrete derivative F'_j(see reference [58]).

Instead of using the constant weights (3.9), the WENO scheme [8] adaptively selects the weights in relation to the "smoothness" of the stencils. The non-linear weights are introduced as

$$\omega_{i,j\pm1/2} = \frac{\gamma_{i,j\pm1/2}}{\sum_{k=0}^{2} \gamma_{k,j\pm1/2}}, \qquad \gamma_{i,j\pm1/2} = \frac{C_i}{(\varepsilon + IS_{i,j\pm1/2})^p}, \qquad i = 0,\, 1,\, 2, \tag{3.11}$$

where ε is a small parameter which prevents the division by zero, p is an integer (set equal to 2 in [8]), C_j are those given in (3.9), and $IS_{i,j\pm1/2}$ are the "smoothness" indicators given in [8]. In general, $IS_{i,j-1/2} \neq IS_{i,j+1/2}$, implying that also $\omega_{i,j-1/2} \neq \omega_{i,j+1/2}$. Note that the non-linear weights need to satisfy $\sum_{k=0}^{2} \omega_{k,j\pm1/2} = 1$ for consistency of the scheme. Using the non-linear weights (3.11) for the combination if the candidates, the final form of the WENO scheme reads as

$$\begin{aligned}
F'_j &= \frac{\hat{F}_{j+1/2} - \hat{F}_{j-1/2}}{h_j} \\
&\approx \left[-\frac{1}{3}\omega_{0,j-1/2} F_{j-3} + \left(\frac{7}{6}\omega_{0,j-1/2} + \frac{1}{3}\omega_{0,j+1/2} + \frac{1}{6}\omega_{1,j-1/2} \right) F_{j-2} \right. \\
&+ \left(-\frac{11}{6}\omega_{0,j-1/2} - \frac{7}{6}\omega_{0,j+1/2} - \frac{5}{6}\omega_{1,j-1/2} - \frac{1}{6}\omega_{1,j+1/2} - \frac{1}{3}\omega_{2,j-1/2} \right) F_{j-1} \\
&+ \left(\frac{11}{6}\omega_{0,j+1/2} - \frac{1}{3}\omega_{1,j-1/2} + \frac{5}{6}\omega_{1,j+1/2} - \frac{5}{6}\omega_{2,j-1/2} + \frac{1}{3}\omega_{2,j+1/2} \right) F_j \\
&+ \left. \left(\frac{1}{3}\omega_{1,j+1/2} + \frac{1}{6}\omega_{2,j-1/2} \frac{5}{6}\omega_{2,j+1/2} \right) F_{j+1} - \frac{1}{6}\omega_{2,j+1/2} F_{j+2} \right] \frac{1}{h_j} \,.
\end{aligned}$$

From a computational point of view, the WENO scheme produces a diagonal matrix of size $N + 1$, where the j-th row contains the $(j - 1/2)$-th numerical flux $\hat{F}_{j-1/2}$. The final value of the derivative F'_j is then obtained using Equation (2.5).

Following this idea, we can derive the following weighted compact scheme.

3.1.3 The Weighted Compact Scheme (WCS)

The basic idea of WCS [32] is to take a weighted average (convex combination) of two third-order and one fourth-order approximations of the numerical flux $\hat{F}_{j+1/2} = H'_{j+1/2}$, each approximation involving the primitive function H and its derivative H'. Similar to the WENO scheme, three candidate stencils of WCS are defined as

$$\begin{aligned}
E_0: \quad & \hat{F}^{(E_0)}_{j+1/2} &\approx\ & \frac{1}{3}F_{j-2} - \frac{7}{6}F_{j-1} + \frac{11}{6}F_j; \\
E_1: \quad & \hat{F}^{(E_1)}_{j+1/2} &\approx\ & -\frac{1}{6}F_{j-1} + \frac{5}{6}F_j + \frac{1}{3}F_{j+1}; \\
E_2: \quad & \hat{F}^{(E_2)}_{j+1/2} &\approx\ & \frac{1}{3}F_j + \frac{5}{6}F_{j+1} - \frac{1}{6}F_{j+2}.
\end{aligned}$$

The approximations for the numerical flux $H'_{j+1/2} = \hat{F}_{j+1/2}$ are obtained making use of compact schemes [1] for the three stencils E_0 and E_1 and E_2 respectively, as

$$\begin{aligned}
E_0: \quad & 2H'_{j-1/2} + H'_{j+1/2} \approx \left(-\frac{1}{2}H_{j-3/2} - 2H_{j-1/2} + \frac{5}{2}H_{j+1/2}\right)\frac{1}{h_j}; \\
E_1: \quad & \frac{1}{4}H'_{j-1/2} + H'_{j+1/2} + \frac{1}{4}H'_{j+3/2} \approx \frac{3(H_{j+3/2} - H_{j-1/2})}{4h_j}; \\
E_2: \quad & H'_{j+1/2} + 2H'_{j+3/2} \approx \left(-\frac{5}{2}H_{j+1/2} + 2H_{j+3/2} + \frac{1}{2}H_{j+5/2}\right)\frac{1}{h_j}.
\end{aligned} \tag{3.12}$$

By a Taylor expansion of Equation (3.12), it can be verified that the candidates and give a third-order approximation of $H'_{j+1/2}$, while the candidate E_1 is of fourth-order accuracy [58]. Similar to WENO, if the following constant weights are chosen,

$$C_0 = \frac{1}{18}, \qquad C_1 = \frac{8}{9}, \qquad C_2 = \frac{1}{18}, \tag{3.13}$$

the weighted average of the three candidate approximations in (3.12) gives the following approximation for $H'_{j+1/2}$,

$$\begin{aligned}
&\frac{1}{3}H'_{j-1/2} + H'_{j+1/2} + \frac{1}{3}H'_{j+3/2} \\
&\approx \left(-\frac{1}{36}H_{j-3/2} - \frac{7}{9}H_{j-1/2} + \frac{7}{9}H_{j+3/2} + \frac{1}{36}H_{j+5/2}\right)\frac{1}{h_j}.
\end{aligned} \tag{3.14}$$

By using equations (3.4 and 3.5), it can be easily shown [58] that equation (3.14) recovers exactly the standard sixth order compact scheme [1]. An analogous procedure leads to the expression for $H'_{j-1/2} = \hat{F}_{j-1/2}$. Instead of the constant weights (3.13), we use the non-linear weights form (3.11) setting the parameter $p = 1$, and apply (3.5) to obtain the expression for the final form of the WCS scheme, which reads as

$$
\begin{aligned}
&-[3(\omega_{0,j-1/2} - \omega_{0,j+1/2}) + \frac{3}{2}(\omega_{1,j-1/2} - \omega_{1,j+1/2}) + 3(\omega_{2,j-1/2} - \omega_{2,j+1/2})]\frac{H'_{j+1/2}}{h_j} + \\
&\left(2\omega_{0,j-1/2} + \tfrac{1}{4}\omega_{1,j-1/2}\right) F'_{j-1} + \left(3\omega_{0,j-1/2} + \frac{5}{4}\omega_{1,j-1/2} + \omega_{2,j-1/2} - 2\omega_{0,j+1/2}\right. \\
&\left. -\frac{1}{4}\omega_{1,j+1/2}\right) F'_j + \left(\frac{1}{4}\omega_{1,j+1/2} + 2\omega_{2,j+1/2}\right) F'_{j+1} \approx \\
&\left[-\frac{1}{2}\,\omega_{0,j-1/2}F_{j-2} + \left(-\frac{5}{2}\omega_{0,j-1/2} - \frac{3}{4}\omega_{1,j-1/2} + \frac{1}{2}\omega_{0,j+1/2}\right) F_{j-1} + \right. \\
&\left(-\frac{3}{4}\omega_{1,j-1/2} - \frac{5}{2}\omega_{2,j-1/2} + \frac{5}{2}\omega_{0,j+1/2} + \frac{3}{4}\omega_{1,j+1/2}\right) F_j + \\
&\left.\left(-\frac{1}{2}\omega_{2,j-1/2} + \frac{3}{4}\omega_{1,j+1/2} + \frac{5}{2}\omega_{2,j+1/2}\right) F_{j+1} + \frac{1}{2}\omega_{2,j+1/2}F_{j+2}\right] \frac{1}{h_j}\ .
\end{aligned}
\tag{3.15}
$$

For the WCS (3.15), a tri-diagonal matrix of size $N + 1$ has to be solved. The j-th row contains the $j - 1/2$-th numerical flux $H'_{j-1/2} = \hat{F}_{j-1/2}$ and the final value of the derivative F'_j is obtained using equation (3.5). The WCS (3.15) involves also the derivatives at different points, F'_{j-1} and F'_{j+1}, thus results in a compact scheme, i.e., the WCS has global dependency.

3.1.4 WENO Scheme with Global Weights

a). CPU comparison

When the original WENO scheme is used in solving the problems, for example, 2D Euler equations, we need to calculate the weights of each stencil at each iteration step for each variable, which has a high cost. To reduce the cost and get better results,

we only calculate the weights of some variables, say, pressure and density, only once, and combine them to be the global weights before carrying out Runge-Kutta time marching method at each time step. Application of global weights will reduce the cost of the computation. We have some comparison of CPU time in solving 2D Euler equations by using original WENO and the new one with global weights as following,

Table 3.1. Comparison of CPU time usage of the two WENO schemes

Grids:	Original WENO	New WENO
33×33	248 s	168 s
65×65	1921 s	1312 s

Here, the mean of the weights for pressure and density is used to be the global weights (proposed by Dr. Chaoqun Liu). Table 3.1 shows us that the global one will reduce CPU time 32% for our 2D code, which accelerates our computation. Although WENO and WENO with global weights capture the shock in a good manner, they are too dissipative in the smooth area. To improve the resolution, WENO with global weights can be combined with the WCS (Weighted Compact Scheme) to be the following Modified Weighted Compact Scheme (MWCS).

b). Convergence rate

The following two figures show that for 2D Euler equation, the WENO scheme with global weights converges faster than WENO scheme with local weights.

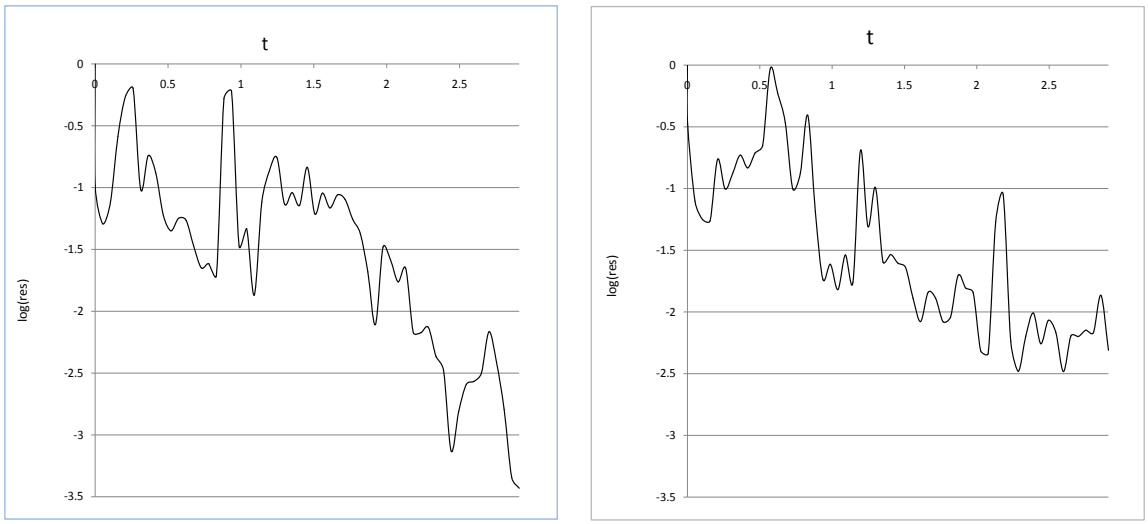

(a) (b)

Figure 3.3. Convergence rate comparison (a) WENO with global weights; (b) WENO with local weights.

3.1.5 The Modified Weighted Compact Scheme (MWCS)

The MWCS combines the two schemes described in the previous sections, WENO and WCS, and it includes the following aspects, first, we move the weights for WENO and WCS outside the derivative subroutine, i.e., using global weights. Second, we use the mean value of the WENO and WCS weights calculated from pressure and density as the weights of the whole scheme for all variables. The weights here only need to be calculated once before carrying out the Runge-Kutta method. Finally, for combining WENO scheme and WCS scheme, a mixing function is used for the mean value of the weights of those four fluxes (two for pressure and two for density).

The mixing function aims to linearly combine the two schemes in order to ensure numerical stability on one hand, and to obtain a sharp shock-capturing and

good resolution for small length scales on the other. The resulting formulation of the MWCS numerical flux reads as

$$\hat{F}_{j-1/2}^{(MWCS)} = (1-\alpha_j)\hat{F}_{j-1/2}^{(WCS)} + \alpha_j \hat{F}_{j-1/2}^{(WENO)}. \tag{3.16}$$

For consistency of the scheme, it is required that $0 \leq \alpha \leq 1$. Virtually, with $\alpha = 1$ the WENO scheme is recovered. Here we choose α as following(proposed by Huankun Fu),

$$\alpha = 1 - 0.5 * \left(1 - \frac{(IS0 - IS1)^2 + (IS1 - IS2)^2 + (IS2 - IS0)^2}{2 * (IS0^2 + IS1^2 + IS2^2)}\right), \tag{3.17}$$

where $IS0, IS1$ and $IS2$ are the smoothness indicators obtained from WENO scheme.

3.1.6 Dispersion and Dissipation Analysis

Fourier analysis of dispersion error and dissipation error in the two publications [53] and [59] provides us an effective insight into resolution and diffusion properties of numerical schemes, hence for MWCS, and possibly can be used to do further research in improving the mixing function proposed in equation (3.17).

Following Vichnevetsky and Bowles [59], the effective wavenumber [59] $\mathrm{i}\widehat{k_e}$ for WENO, WCS and MWCS need to be calculated, where i is the imaginary unit $\mathrm{i} = \sqrt{-1}$. Practically, we suppose $\omega_{i,j-1/2} = \omega_{i,j+1/2} = \omega_i$ in WENO, WCS and MWCS. For MWCS, the linear combination weight function α in equation (3.17) is not constant, which is not suitable for performing dispersion and dissipation analysis, hence it is assumed to be constant for references.

The effective wavenumber $\mathrm{i}\widehat{k_e}$ of WENO scheme, following Vichnevetsky and Bowles [59], can be calculated as

$$\begin{aligned}\mathrm{i}\,\widehat{k}_e^{(\mathrm{WENO})} = &\frac{11}{6}\omega_0 + \frac{1}{2}\omega_1 - \frac{1}{2}\omega_2 + \left(-3\omega_0 - \frac{2}{3}\omega_1 + \frac{2}{3}\omega_2\right)\cos\widehat{k} + \\ &\left(\frac{3}{2}\omega_0 - \frac{1}{6}\omega_1 - \frac{1}{6}\omega_2\right)\cos 2\widehat{k} - \frac{1}{3}\omega_0\cos 3\widehat{k} + \\ &\mathrm{i}\left[\left(3\omega_0 + \frac{4}{3}\omega_1 + \frac{4}{3}\omega_2\right)\sin\widehat{k} + \right. \\ &\left.\left(-\frac{3}{2}\omega_0 - \frac{1}{6}\omega_1 - \frac{1}{6}\omega_2\right)\sin 2\widehat{k} + \frac{1}{3}\omega_0\sin 3\widehat{k}\right].\end{aligned} \tag{3.18}$$

Similarly, the effective wavenumber of WCS is

$$\begin{aligned}\mathrm{i}\,\widehat{k}_e^{(\mathrm{WCS})} = &\left[(\omega_0 - \omega_2)\left(5 - 4\cos\widehat{k} - \cos 2\widehat{k}\right) + \right. \\ &\left.\mathrm{i}\left((4\omega_0 + 3\omega_1 + 4\omega_2)\sin\widehat{k} + (\omega_0 + \omega_2)\sin 2\widehat{k}\right)\right] \Big/ \\ &\left[(4\omega_0 + \omega_1 + 4\omega_2)\cos\widehat{k} + 2\left(\omega_0 + \omega_1 + \omega_2\right) - 4\mathrm{i}\left(\omega_0 - \omega_2\right)\sin\widehat{k}\right].\end{aligned} \tag{3.19}$$

The dispersion error, or the resolution of the scheme, may be quantified by the imaginary part of the effective wavenumber $\mathrm{Im}(\mathrm{i}\hat{k}_e)$, while the real part $\mathrm{Re}(\mathrm{i}\hat{k}_e)$ is related to dissipation. Dispersion errors are waves, corresponding to different wavenumbers, which travel at different velocity. The imaginary part of the effective wavenumber $\mathrm{Im}(\mathrm{i}\hat{k}_e)$ represents dispersion, i.e., the phase error in representing the different wavenumbers of the spectrum. Dissipation or diffusion errors, associated to the negative of the real part of the effective wavenumber $\mathrm{Re}(\mathrm{i}\hat{k}_e)$, constitute the amplification error, either positive or negative, which is introduced by the numerical scheme.

The following subsections discuss the Fourier analysis of the dispersion and dissipation in smooth region and shock region when using WENO, WCS and MWCS, the linear combination function is assumed to be $0.1, 0.4$ and 0.8 for references.

3.1.6.1 Smooth regions

For smooth region, we only need to consider optimal weights in WENO, WCS and MWCS, that is (3.9), (3.13) or both of them, respectively. Put these weights into the expressions of effective wavenumbers (3.18) and (3.19).

For the dispersion error, the imaginary parts of the resulting effective wavenumbers have to be considered, i.e.,

$$\mathrm{Im}\left(\mathrm{i}\,\widehat{k}_e^{(\mathrm{WENO})}\right) = \frac{3}{2}\sin\widehat{k} - \frac{3}{10}\sin 2\widehat{k} + \frac{1}{30}\sin 3\widehat{k}; \tag{3.20a}$$

$$\mathrm{Im}\left(\mathrm{i}\,\widehat{k}_e^{(\mathrm{WCS})}\right) = \frac{\left(14+\cos\widehat{k}\right)\sin\widehat{k}}{9+6\cos\widehat{k}}. \tag{3.20b}$$

Figures 3.4(a) shows that

- MWCS is of higher resolution than WENO on smooth region;
- WCS achieves the highest resolution of the three.

Similarly, dissipation error can be derived by considering real parts of (3.18) and (3.19), which read as

$$\mathrm{Re}\left(\mathrm{i}\,\widehat{k}_e^{(\mathrm{WENO})}\right) = \frac{1}{3} - \frac{1}{2}\cos\widehat{k} + \frac{1}{5}\cos 2\widehat{k} - \frac{1}{30}\cos 3\widehat{k}; \tag{3.21a}$$

$$\mathrm{Re}\left(\mathrm{i}\,\widehat{k}_e^{(\mathrm{WCS})}\right) = 0. \tag{3.21b}$$

Figures 3.4(b) presents the comparison of dissipation error, and it can be concluded that

- WCS is characterized by absence of dissipation error;
- WENO scheme if of highest dissipation error of high range of wavenumber $\widehat{k}$;
- MWCS is of low dissipation error over the middle and high wavenumber range.

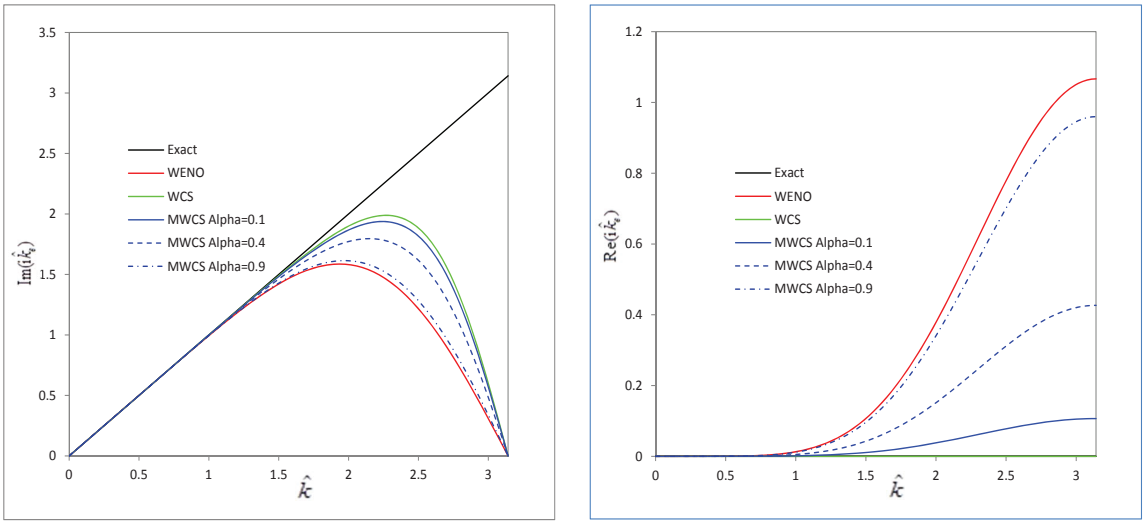

(a) (b)

Figure 3.4. Error analysis in smooth region (a) dispersion; (b) dissipation.

3.1.6.2 Shock region: using only stencil E_0

We assume that the stencils E_1 and E_2 defined in section 3.8 contain shocks, therefore we substitute the following values of the linear weights

$$\omega_0 = 1, \quad \omega_1 = \omega_2 = 0 \tag{3.22}$$

into the expressions of effective wavenumbers (3.19) and (3.19) for WENO and WCS, respectively.

The dispersion errors are

$$\mathrm{Im}\left(\mathrm{i}\,\widehat{k}_e^{(\mathrm{WENO})}\right) = 3\sin\widehat{k} - \frac{3}{2}\sin 2\widehat{k} + \frac{1}{3}\sin 3\widehat{k}; \tag{3.23a}$$

$$\mathrm{Im}\left(\mathrm{i}\,\widehat{k}_e^{(\mathrm{WCS})}\right) = \frac{\left(8+\cos\widehat{k}\right)\sin\widehat{k}}{5+4\cos\widehat{k}}. \tag{3.23b}$$

And the dissipation errors become

$$\mathrm{Re}\left(\mathrm{i}\,\widehat{k}_e^{(\mathrm{WENO})}\right) = \frac{11}{6} - 3\cos\widehat{k} + \frac{3}{2}\cos 2\widehat{k} - \frac{1}{3}\cos 3\widehat{k}; \tag{3.24a}$$

$$\mathrm{Re}\left(\mathrm{i}\,\widehat{k}_e^{(\mathrm{WCS})}\right) = -\frac{4\sin\left(\widehat{k}/2\right)^4}{5+4\cos\widehat{k}}. \tag{3.24b}$$

The following two figures 3.5(a) and 3.5(b) show us that

- WENO is of lowest resolution, while MWCS is better and better as α decreasing, and WCS is of highest resolution;
- WENO scheme is dissipative predominantly over high wavenumber range, but WCS is negatively dissipative at high wavenumber range, MWCS, on other hand, tends to have lower dissipative error than WENO scheme.

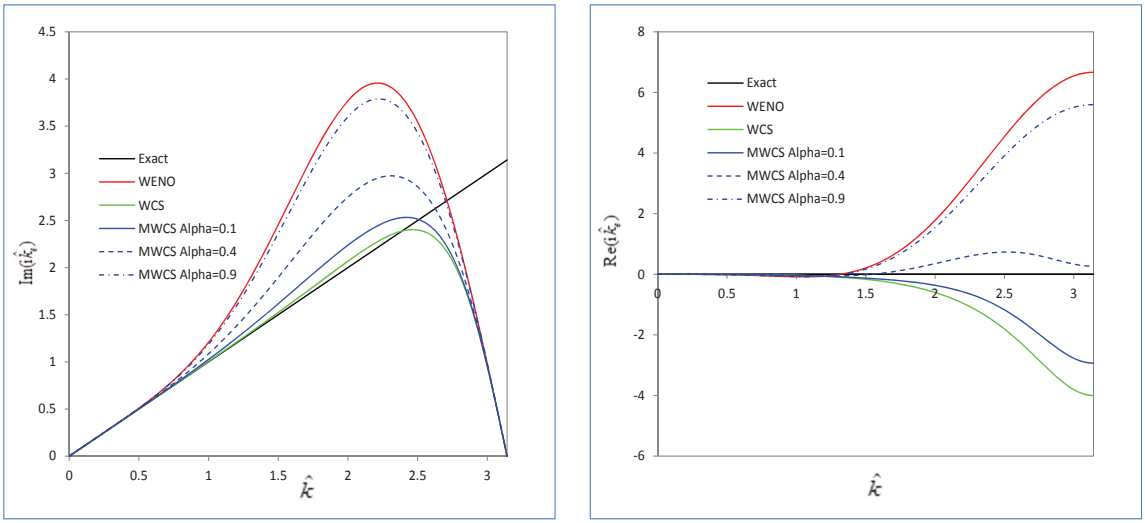

(a) (b)

Figure 3.5. Error analysis in in stencil E_0 (a) dispersion; (b) dissipation.

3.1.6.3 Shock region: using only stencil E_1

In this case, we assume that the stencils E_0 and E_2 contain shocks, therefore assume the weights,

$$\omega_0 = 0, \quad \omega_1 = 1, \quad \omega_2 = 0, \tag{3.25}$$

which induce the following dispersion errors

$$\mathrm{Im}\left(\mathrm{i}\,\widehat{k}_e^{(\mathrm{WENO})}\right) = \frac{4}{3}\sin\widehat{k} - \frac{1}{6}\sin 2\widehat{k}; \tag{3.26a}$$

$$\mathrm{Im}\left(\mathrm{i}\,\widehat{k}_e^{(\mathrm{WCS})}\right) = \frac{3\sin\widehat{k}}{2+\cos\widehat{k}}, \tag{3.26b}$$

and the following dissipation errors

$$\mathrm{Re}\left(\mathrm{i}\,\widehat{k}_e^{(\mathrm{WENO})}\right) = \frac{1}{2} - \frac{2}{3}\cos\widehat{k} + \frac{1}{6}\cos 2\widehat{k}; \tag{3.27a}$$

$$\mathrm{Re}\left(\mathrm{i}\,\widehat{k}_e^{(\mathrm{WCS})}\right) = 0. \tag{3.27b}$$

The next two figures 3.6(a) and 3.6(b) demonstrate the conclusions that

- On stencil E_1, the resolution of WENO scheme is confined to the low wavenumber range;
- MWCS is better than WENO in resolution, while WCS is the best;
- WCS assumes no dissipative error which is better than MWCS, while WENO scheme is of the most dissipative one.

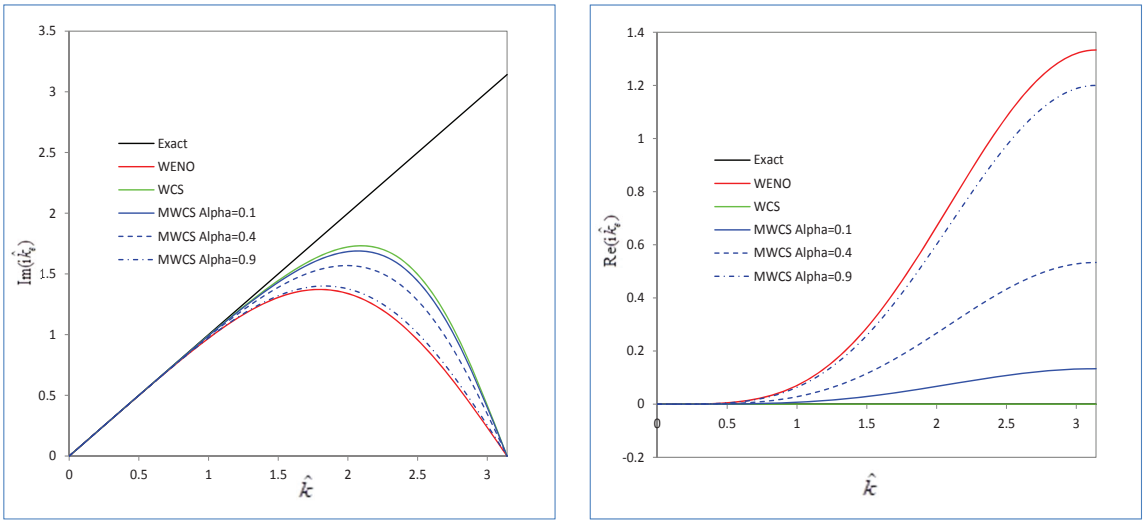

(a) (b)

Figure 3.6. Error analysis in in stencil E_1 (a) dispersion; (b) dissipation.

3.1.6.4 Shock region: using only stencil E_2

This last case deals with the stencil E_2, i.e., considering the case that E_0 and E_1 contain shocks. Hence the following weights should be assumed,

$$\omega_0 = \omega_1 = 0, \quad \omega_2 = 1. \tag{3.28}$$

The corresponding dispersion errors become

$$\mathrm{Im}\left(\mathrm{i}\,\widehat{k}_e^{(\mathrm{WENO})}\right) = \frac{4}{3}\sin\widehat{k} - \frac{1}{6}\sin 2\widehat{k}; \tag{3.29a}$$

$$\mathrm{Im}\left(\mathrm{i}\,\widehat{k}_e^{(\mathrm{WCS})}\right) = \frac{\left(8+\cos\widehat{k}\right)\sin\widehat{k}}{5+4\cos\widehat{k}}, \tag{3.29b}$$

and the dissipative errors are

$$\mathrm{Re}\left(\mathrm{i}\,\widehat{k}_e^{(\mathrm{WENO})}\right) = -\frac{1}{2} + \frac{2}{3}\cos\widehat{k} - \frac{1}{6}\cos 2\widehat{k}; \tag{3.30a}$$

$$\mathrm{Re}\left(\mathrm{i}\,\widehat{k}_e^{(\mathrm{WCS})}\right) = \frac{4\sin\left(\widehat{k}/2\right)^4}{5 + 4\cos\widehat{k}}. \tag{3.30b}$$

The following two figures 3.7(a) and 3.7(b) show us that

- MWCS has improved the resolution with respect to WENO scheme, as α decreases, while WCS achieves the highest resolution;
- On stencils E_1 and E_2, WENO scheme has the same resolution. Meanwhile, on stencils E_0 and E_2, MWCS has the same resolution;
- WENO shceme is negatively dissipated at middle and high wavenumber range, while WCS is positively dissipated. The combination of them, MWCS, achieves smaller dissipation error with respect to both WENO and WCS;
- On stencils E_1 and E_2, WENO scheme has the equal dissipation error, but with opposite signs. Meanwhile, on stenicls E_0 and E_2, WCS achieves the same property.

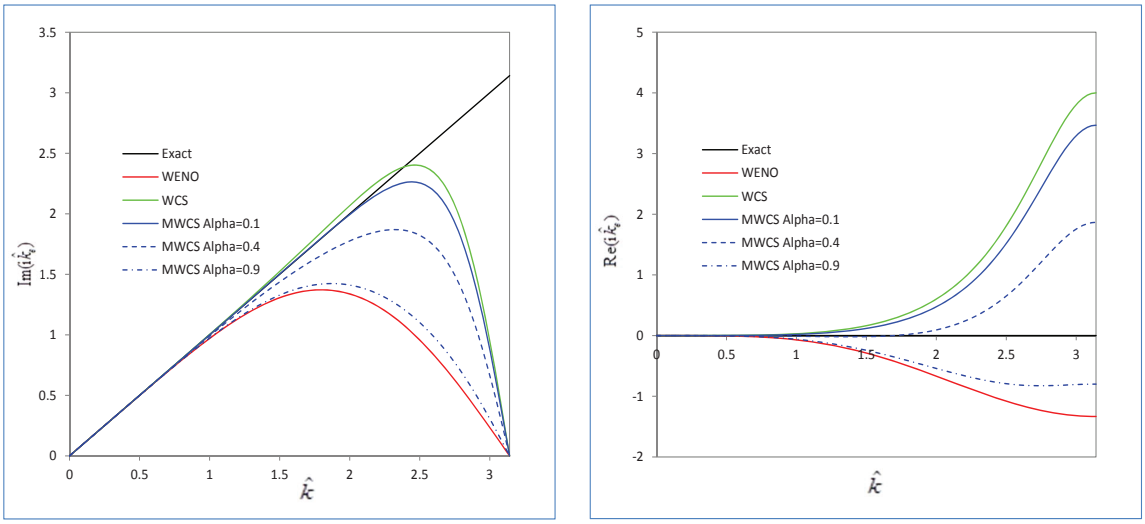

(a) (b)

Figure 3.7. Error analysis in in stencil E_2 (a) dispersion; (b) dissipation.

3.2 Numerical Results

The Euler equations for selected one- and two-dimensional test cases are solved by the proposed MWCS and compared with using WENO [8].

3.2.1 One-dimensional Case

The one-dimensional Euler equations in vector and conservative form read as

$$\begin{aligned} &\frac{\partial U}{\partial t} + \frac{\partial F}{\partial x} = 0, \\ &U = (\rho,\, \rho u,\, E_t)^T, \\ &F = (\rho u,\, \rho u^2 + p,\, u(E_t + p))^T, \end{aligned} \tag{3.31}$$

where $x \in (-5, 5)$, and the grid is uniform with size $h = 0.05$ (201 grid points). Steger-Warming [54] flux-splitting is used, and the time marching uses third-order Runge-Kutta scheme.

3.2.1.1 Sod shock-tube problem

The shock-capturing capability of the MWCS is tested by the Sod shock-tube problem [45]. Equations (3.31) are solved coupled with the following initial conditions,

$$(\rho,\, u,\, p) = \begin{cases} (1,\, 0,\, 1), & t = 0,\, x \leq 0; \\ (0.125,\, 0,\, 0.1), & t = 0,\, x > 0. \end{cases} \tag{3.32}$$

Figure 3.8(a) to Figure 3.8(d) show the plots of the solved velocity u, at time $t = 2$. Figure 3.8(a) and Figure 3.8(b) report the solution in the whole domain for MWCS and WENO schemes, respectively. The reference solution is regarded as the one obtained by the fifth - order WENO scheme using a mesh of 1601 points, labeled as WENO 1601. All the other simulations are carried out on a coarser mesh of 201 points. The solutions using MWCS (labeled as MWCS 201) and WENO scheme (labeled as WENO 201) are free from visible oscillations, which is different from using WCS. Figure 3.8(c) and Figure 3.8(d) report the enlargements of the shock areas, comparing the three different schemes. Using MWCS scheme, the discontinuity is captured more sharply and is less smeared compared to using the fifth-order WENO, and the solution does not have visible oscillations.

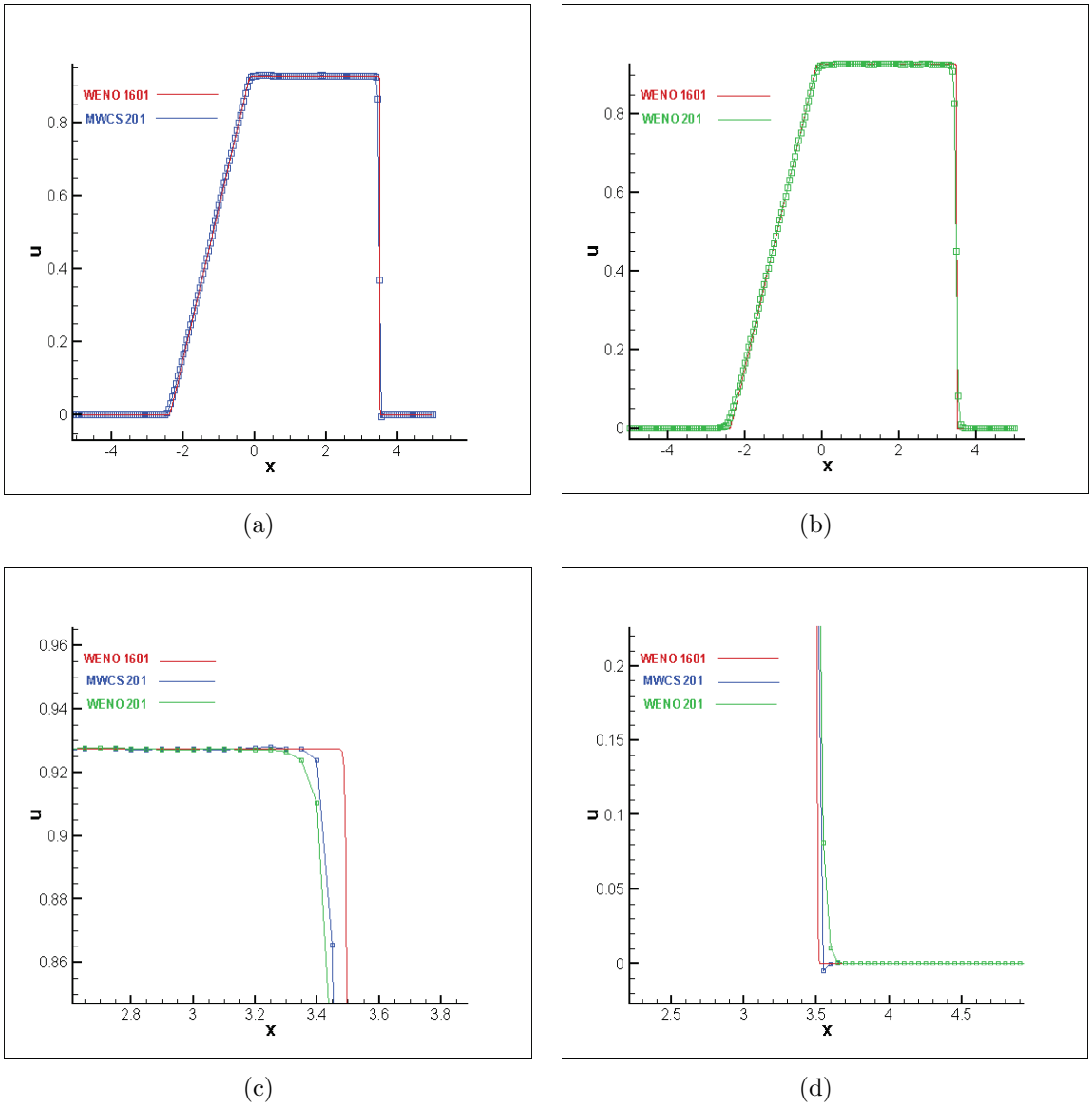

Figure 3.8. Solution to shock tube problem (a) MWCS; (b) WENO; (c) enlarged comparison; (d) enlarged comparison.

3.2.1.2 Shu-Osher Problem

The shock-entropy wave interaction problem (Shu and Osher, Efficient implementation of essentially non-oscillatory shock-capturing schemes II 1989) is solved

in order to test the proposed method's capability on shock-capturing and shock-turbulence interaction. The entropy waves are very sensitive to numerical dissipation introduced by a numerical scheme, and can be excessively damped. Equations (3.31) are solved, coupled with the following initial condition,

$$(\rho,\, u,\, p) = \begin{cases} (3.857143,\, 2.629369,\, 10.33333), & t = 0,\, x < -4; \\ (1 + 0.2\sin(5x),\, 0,\, 1), & t = 0,\, x \geq -4. \end{cases} \tag{3.33}$$

Figure 3.9 shows the result for the solved pressure distribution p at time $t = 18$ by using MWCS and WENO respectively. Figures 3.10 - 3.12 are the comparisons of the results for the solved density distribution ρ. The reference solution is regarded as the one obtained by the fifth-order WENO scheme using a mesh of 1601 points, labeled as WENO 1601. All the other calculations are made on a coarser mesh of 201 points. The MWCS scheme (labeled MWCS 201) shows higher resolution and sharper shock capturing compared with WENO (labeled WENO 201). Figures 3.11 and 3.12 report detailed enlargements of discontinuity areas in the shock region, comparing the two different schemes. The results obtained by using WCS has numerical oscillations. However, it can be observed that the MWCS solution is free from numerical oscillations, able to sharply capture the shock and has better resolution properties than the solution obtained by using WENO.

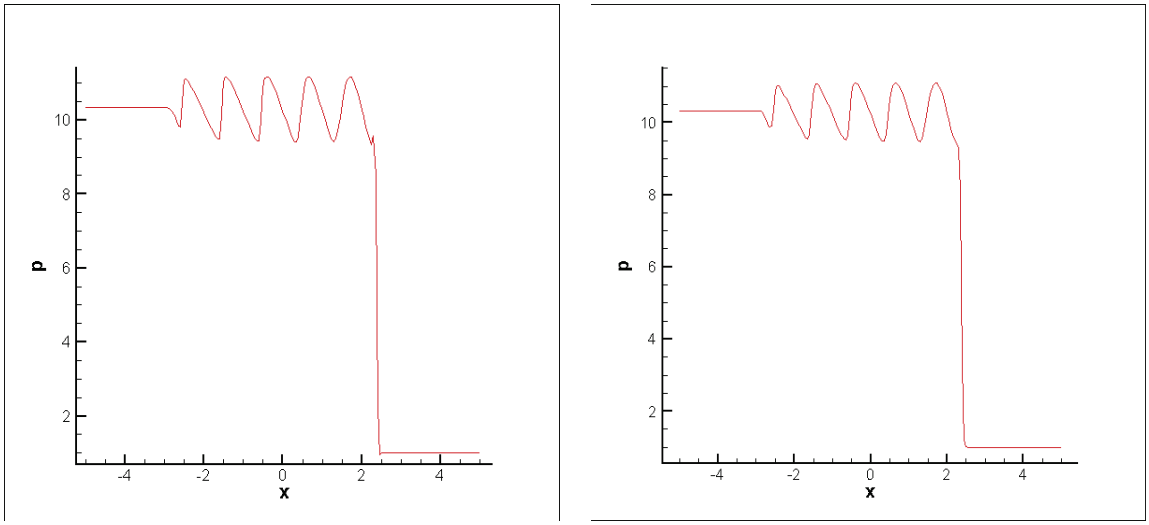

(a) (b)

Figure 3.9. Solution of pressure to Shu-Osher problem (a) MWCS; (b) WENO.

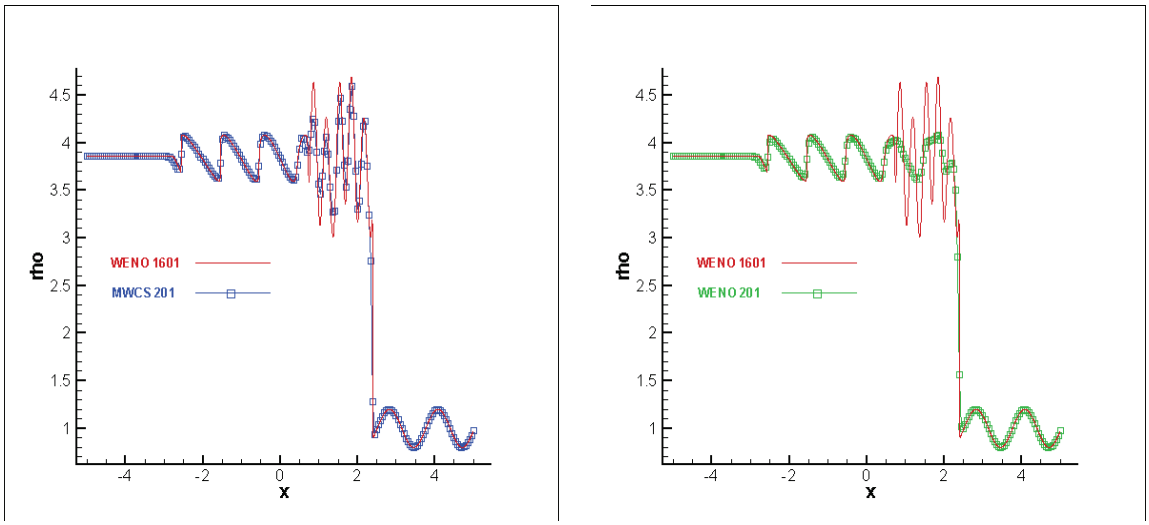

(a) (b)

Figure 3.10. Solution of density to Shu-Osher problem (a) MWCS; (b) WENO.

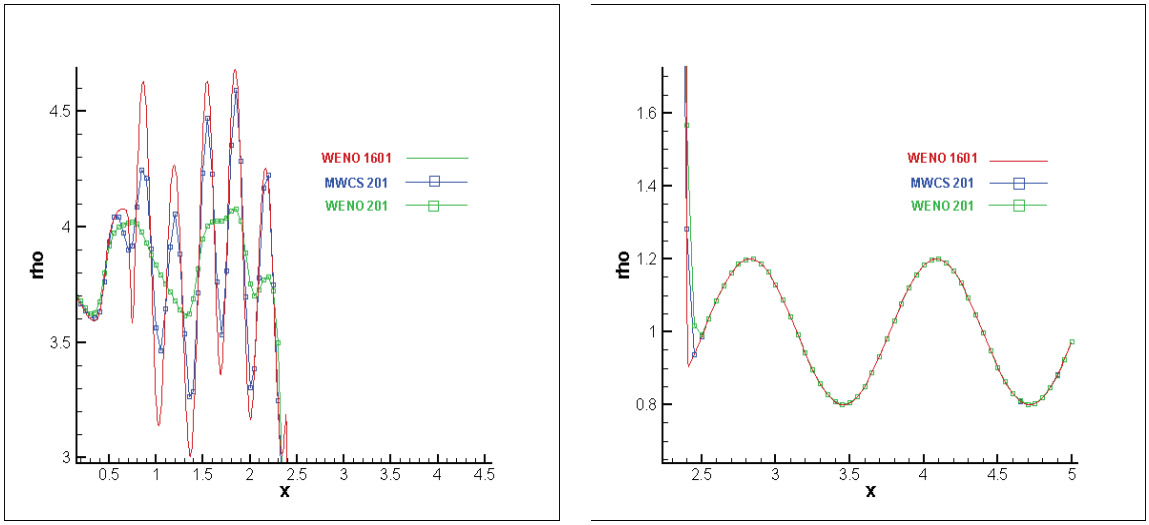

(a) (b)

Figure 3.11. Enlarged solution of pressure to Shu-Osher problem (a) MWCS; (b) WENO.

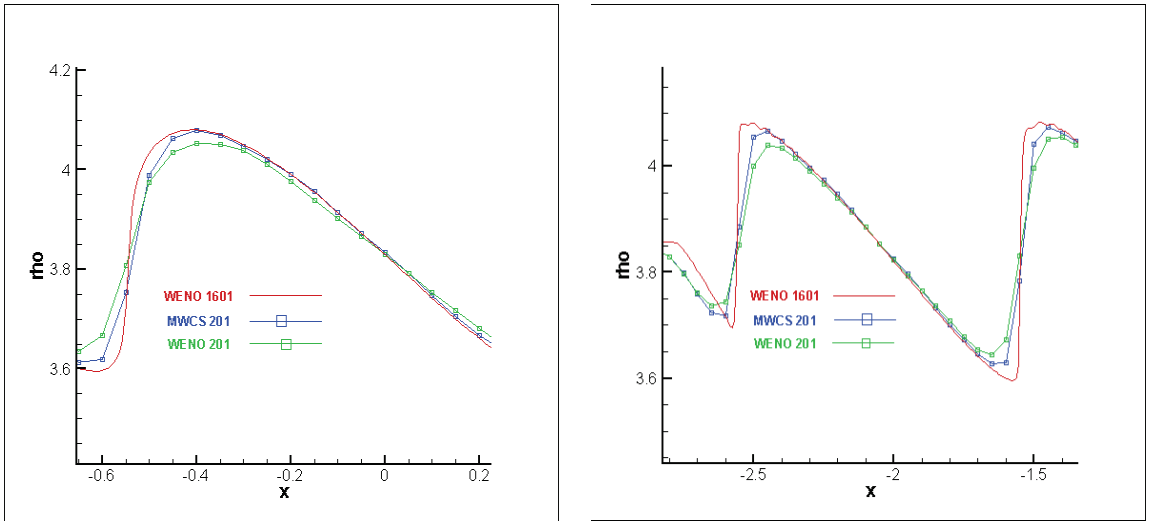

(a) (b)

Figure 3.12. Enlarged solution of pressure to Shu-Osher problem (a) MWCS; (b) WENO.

3.2.1.3 Two Interacting Blast Waves

The interaction of two blast waves was considered in [4] and [68], and is considered here using WENO and MWCS. The initial data are

$$\mathbf{u}(x,0) = \begin{cases} \mathbf{u}_L, & 0 \le x \le 0.1; \\ \mathbf{u}_M, & 0.1 < x \le 0.9; \\ \mathbf{u}_R, & 0.9 < x \le 1. \end{cases}$$

where,

$$\rho_L = \rho_M = \rho_R = 1, u_L = u_M = u_R = 0, \rho_L = 10^3, \rho_M = 10^{-2}, \rho_R = 10^2.$$

In the following solution figures, the reference solution is obtained by using WENO scheme with grid number 2400, and the other use grid 200, 400 respectively. The solution is examined at t=0.038. It is observed that the solution obtained by using MWCS are better than by applying WENO, and the former one is sharper than the later one.

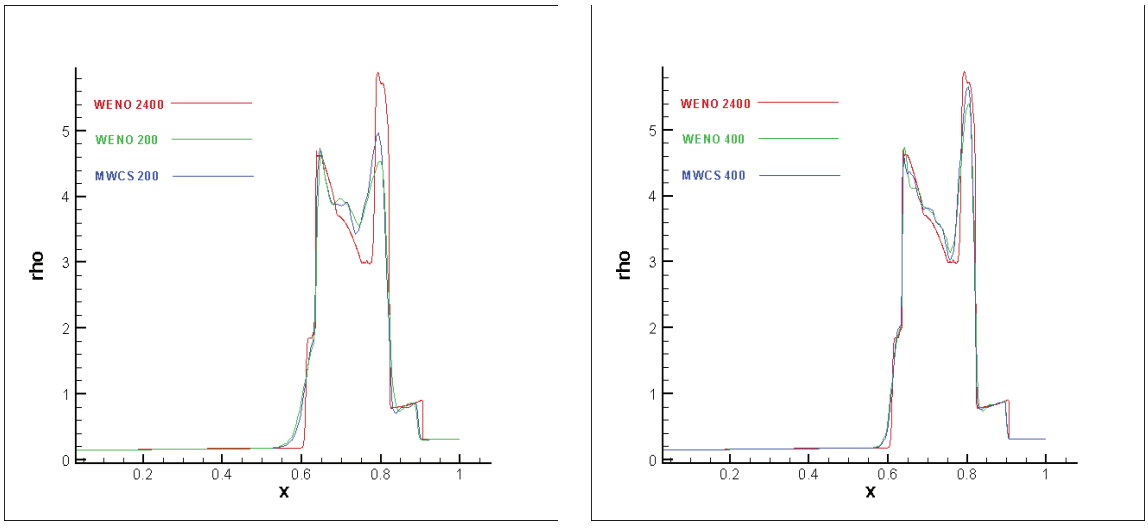

(a) (b)

Figure 3.13. Density solution comparison, 2 interacting blast waves (a) grids: 200; (b) grids: 400.

3.2.2 Two-dimensional Case

The two-dimensional Euler equations in vector and conservative form read as,

$$\begin{aligned} &\frac{\partial \mathbf{U}}{\partial t} + \frac{\partial \mathbf{F}}{\partial x} + \frac{\partial \mathbf{G}}{\partial y} = 0, \\ &\mathbf{U} = (\rho,\, \rho u,\, \rho v,\, E_t)^T, \\ &\mathbf{F} = (\rho u,\, \rho u^2 + p,\, \rho uv, u\,(E_t + p))^T, \\ &\mathbf{G} = (\rho v,\, \rho uv,\, \rho v^2 + p, v\,(E_t + p))^T\,, \end{aligned} \tag{3.34}$$

where $x \in (0, 2)$, $y \in (0, 1.1)$, and a uniform grid of 65×65 points is used. The Lax-Friedrichs flux-splitting is used, and the time marching is a third-order TVD Runge-Kutta scheme. The test case is set up as an oblique shock reflection on an inviscid wall, with shock angle of 35.24^o and the Mach 2 freestream. The non-reflecting upper boundary conditions and the slip-wall conditions at the lower boundary are imposed, the inflow conditions are specified to the freestream and the outflow conditions are calculated by extrapolation. Figures 3.16(a) to 3.17(b) show the distribution of the pressure p, for the analytical, MWCS and WENO solutions respectively (the WCS excessive numerical oscillations prevent from getting a solution in this test case). Comparing the two schemes, it is observed that the MWCS captures the shock more sharply than WENO scheme, and it does not present visible numerical oscillations.

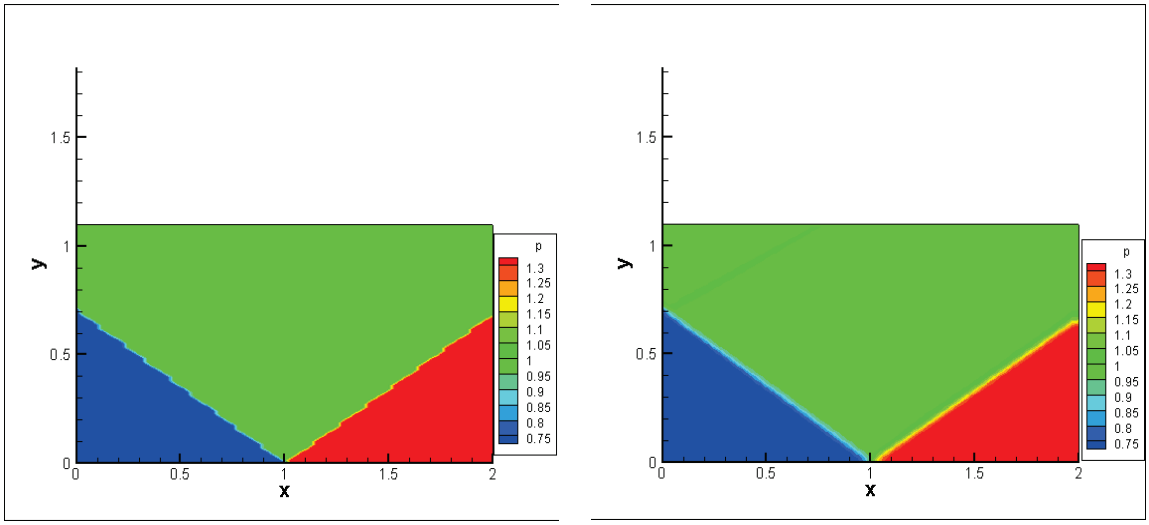

(a) (b)

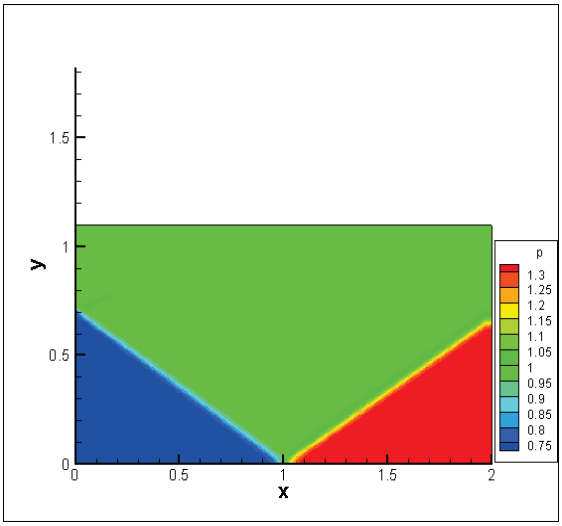

(c)

Figure 3.14. Solution contour pressure of oblique shock reflection (a) analytic solution; (b) by MWCS; (c) by WENO.

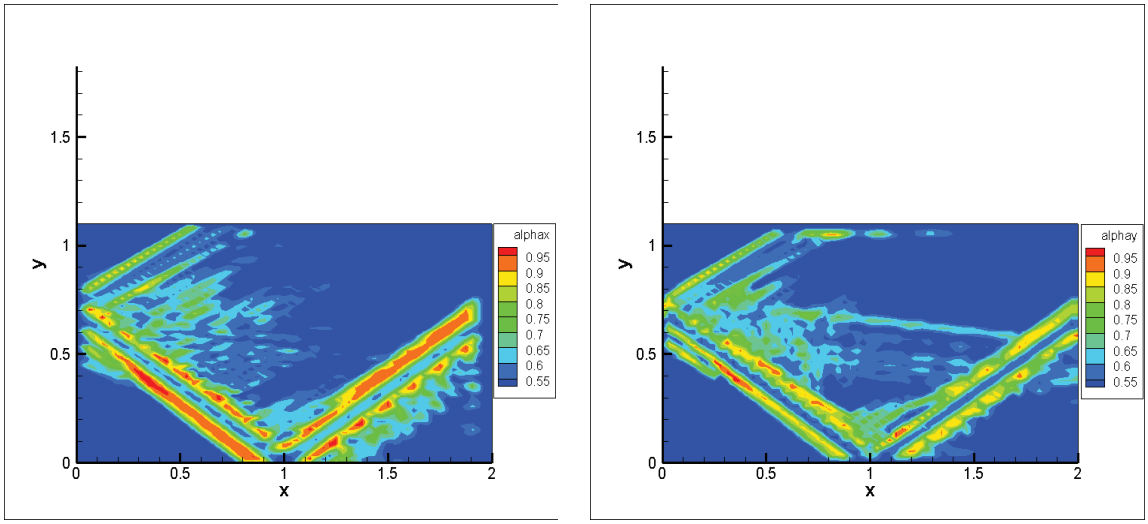

(a) (b)

Figure 3.15. α distribution on 2D grids (a) x direction; (b) y direction.

Figures 3.16(a) and 3.16(b) report the pressure distribution for the Mach 2 oblique shock reflection for $y = 0$ and $y = 0.34$, respectively, for the analytical solution, MWCS and WENO. We can observe that the MWCS can capture the shock sharper than WENO, without generating visible numerical oscillations. Enlargements of shock regions for the pressure distribution at $y = 0.34$ are reported in Figures 3.17(a) and 3.17(b), confirming that MWCS smears the shock less than WENO, without generating visible numerical oscillations.

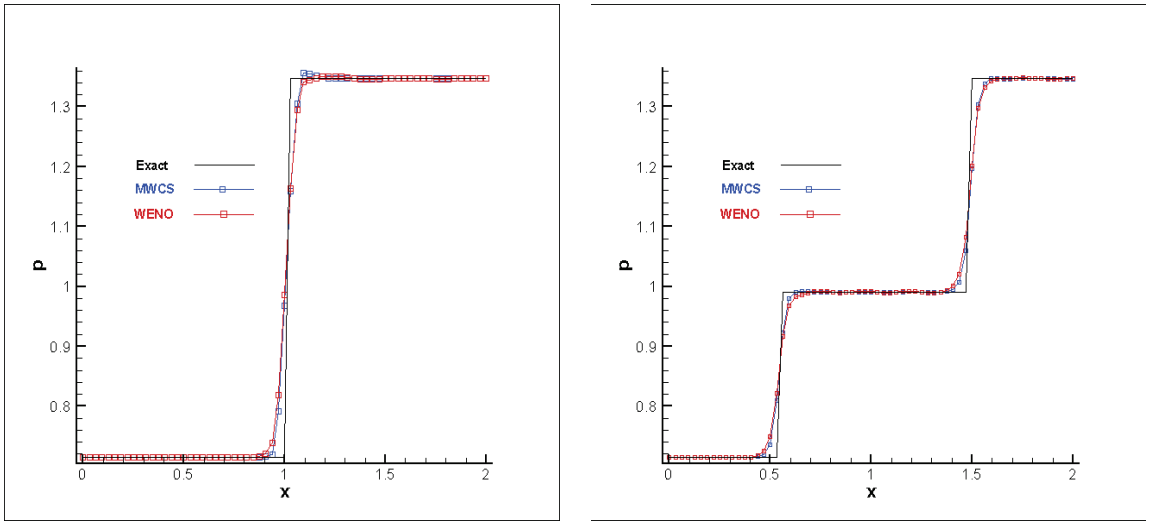

(a) (b)

Figure 3.16. Pressure distribution (a) $y = 0$; (b) $y = 0.34$.

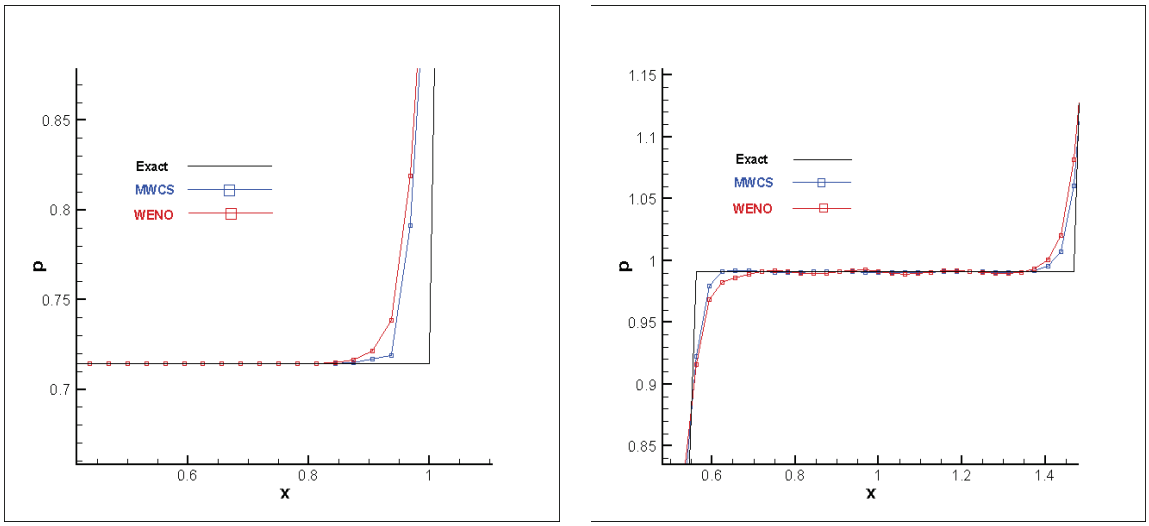

(a) (b)

Figure 3.17. Enlarged pressure distribution (a) $y = 0$; (b) $y = 0.34$.

3.3 Conclusion Remarks

The introduction of so-called "global WENO weights" which uses the mean value of the weights calculated for density and pressure, is found able to reduce the CPU cost largely and make the computation converge fast due to the consistency. The basic formulation of the MWCS, which is a linear combination of the WCS and WENO schemes, is found capable to capture shock and small length scales better than standard WENO. A new formulation of the mixing function based on the smoothness is used, showing that the proposed MWCS has higher resolution and lower dissipation compared to the well established WENO scheme. More important, the new scheme reduced the computation cost dramatically. Numerical tests carried out for inviscid flow problems in one- and two-dimensional cases demonstrates that the proposed method is capable to capture the shock sharply without the generation of visible numerical oscillations.

CHAPTER 4

CONCLUSION AND DISCUSSION

Two high-order algorithms, buffered Fourier spectral method (BFSM) and modified weighted compact scheme (MWCS) are consided for applications in solving PDEs, especially in CFD.

BFSM has been introduced in this dissertation, and it is used to solve the tough problem of using Fourier spectral method to get derivative of a non-periodic function and further applications in solving partial differential equations with non-periodic boundary condition. From this dissertation, it is concluded that BFSM is a scheme with high order accuracy and high resolution. The main idea is to add a periodic orienting buffer region to the non periodic boundary, and then use Fourier spectral method which is of high order accuracy and high resolution, that's why BFSM preserves the same property.

BFSM now only can be used to smooth or nearly smooth function, while MWCS introduced in this dissertation can be applied to problems with shock or large gradient. From Chapter 3, MWCS is a linear combination of WENO and WCS by a mixing function accompanies with using the global weights within the scheme. Dispersion and dissipation analysis of WENO, WCS and MWCS is carried out in Chapter 3, which shows us that MWCS combines the merits of WENO and WCS, that is less dissipative, less dispersive and shock friendly.

The future problems encountered here are the following,

- How to adjust BFSM so that it can be applied to problems with shock or large gradient;

- Further study about how to set a mixing function according the the dispersion and dissipation analysis to make MWCS much more efficient, i.e., with better resolution and less dissipation.

REFERENCES

[1] S. K. Lele, "Compact finite difference schemes with spectral-like resolution". *Journal of Computational Physics*, Vol. 103, pp. 16-42, 1992.

[2] M. Visbal and D. Gaitonde, "On the use of higher-order finite-difference schemes on curvilinear and deforming meshes". *Journal of Computational Physics*, Vol. 181, pp. 155-158, 2002.

[3] H. C. Yee, "Explicit and implicit multidimensional compact high-resolution shock-capturing methods: formulation". *Journal of Computational Physics*, Vol. 131, pp. 216-232, 1997.

[4] C. W. Shu and S. Osher, "Efficient implementation of essentially non-oscillatory shock-capturing scheme". *Journal of Computational Physics*, Vol. 77, pp. 439-471, 1988.

[5] C. W. Shu and S. Osher, "Efficient implementation of essentially non-oscillatory shock-capturing schemes II". *Journal of Computational Physics*, Vol. 83, pp. 32-78, 1989.

[6] A. Harten, B. Engquist, S. Osher and S. R. Chakravarthy, "Uniformly high order accurate essentially non-oscillatory schemes, III". *Journal of Computational Physics*, Vol. 131, pp. 3-47, 1997.

[7] D. Liu, S. Osher, S and T. Chan, "Weighted essentially non-oscillatory schemes". *Journal of Computational Physics*, Vol. 115, pp. 200-212, 1994.

[8] G. S. Jiang and C. W. Shu, "Efficient implementation of weighted ENO scheme". *Journal of Computational Physics*, Vol. 126, pp. 202-228, 1996.

[9] C. W. Shu, "High oder weighted essentially non-oscillatory schemes for convection dominated problems". *SIAM Review*, Vol. 51, pp. 82-126, 2009.

[10] B. Cockburn, S. Y. Lin and C. W. Shu, "TVB Runge-Kutta local projection discontinuous Galerkin finite element method for conservation laws III: one-dimensional systems". *Journal of Computational Physics*, Vol. 84, pp. 90-113, 1989.

[11] B. Cockburn and C. W. Shu, "The local discontinuous Galerkin method for time-dependent convection-diffusion systems". *SIAM Journal on Numerical Analysis*, Vol. 35, pp. 2440-2463, 1998.

[12] F. Bassi and S. Rebay, "A high-order accurate discontinuous finite element menthod for the numerical solution of the compressible Navier-Stokes equations". *Journal of Computational Physics*, Vol. 131, pp. 267-279, 1997.

[13] S. A. Orszag, "A comparison of pseudospectral and spectral approximations". *Stud. Appl. Math.*, Vol. 51, pp. 253-259, 1972.

[14] A. Patera, "A spectral element method for fluid dynamics: Laminar flow in a channel expansion". *Journal of Computational Physics*, Vol. 54, pp. 468-488, 1984.

[15] Z. Wang and G. P. Huang, "An essentially non-oscillatory high-order Padé-type (ENO-Padé) scheme". *Journal of Computational Physics*, Vol. 177, pp. 37-58, 2002.

[16] Y. Liu, M. Vinokur and Z. J. Wang, "Spectral (finite) volume method for conservation laws on unstructured grids. V: extension to three-dimensional systems". *Journal of Computational Physics*, Vol. 212, pp. 454-472, 2006.

[17] Y. Liu, M. Vinokur and Z. J. Wang, "Spectral difference method for unstructured grids I: basic formulation" *Journal of Computational Physics*, Vol. 216, pp. 780-801, 2006.

[18] Y. Sun, Z. J. Wang and Y. Liu, "High-order multi-domain spectral difference method for the Navier-Stokes equations on unstructured hexahedral grids". *Communications in Computational Physics*, Vol. 2, pp. 310-333, 2007.

[19] H. C. Yee, B. Sjogreen, N. D. Sandham and A. Hadjadj, "Progress in the development of a class of efficient low dissipative high order shock-capturing methods". *Proceeding of the Symposium in Computational Fluid Dynamics for the 21st Century*, Kyoto, 2000.

[20] Y. Ma and D. Fu, "Fourth order accurate compact scheme with group velocity control (GVC)". *Science in China*, Vol. 44, pp. 1197-1204, 2001.

[21] N. A. Adams and K. Shariff, "A high-resolution hybrid compact-ENO scheme for shock-turbulence interaction problems". *Journal of Computational Physics*, Vol. 127, pp. 27-51, 1996.

[22] Z. J. Wang, "Spectral (finite) volume method for conservation laws on unstructured grids: basic formulation". *Journal of Computational Physics*, Vol. 178, pp. 210-251, 2002.

[23] J. P. Boyd, *Chebyshev and Fourier spectral methods*. Dover, New York, 2001.

[24] P. Schlatter, N. A. Adams and L. Kleiser, "A windowing method for periodic inflow/outflow boundary treatment of non-periodic flows". *Journal of computational physics*, Vol. 206, pp. 505-535, 2005.

[25] J. Wang, "Finite spectral method based on non-periodic Fourier transform". *Computer & Fluids*, Vol 27, Hos 5-6, pp. 639-644, 1998.

[26] M. Taylor, J. Tribbia and M. Iskandarani, "The Spectral Element Method for the Shallow Water Equations on the Sphere". *Journal of Computational Physics*, Vol. 130(1), pp. 92-108, 1997.

[27] S. K. Godunov, "A difference method for numerical calculation of discontinuous solutions of the equations of hydrodynamics". *Mat. Sb. (N.S.)*, Vol. 47, pp. 271-306, 1959.

[28] P. L. Roe, "Approximate Riemann solvers, parameter vectors, and difference schemes". *Royal Aircraft Establishment*, Bedford, United Kingdom, pp. 357-372, 1981.

[29] B. van Leer, "Towards the ultimate conservative difference scheme V. A second-order sequel to Godunov's method". *Journal of Computational Physics*, Vol. 135, pp. 229-248, 1997.

[30] D. Kim and J. Kwon, "A high-order accurate hybrid scheme using a central flux scheme and a WENO scheme for compressible flowfield analysis". *Journal of Computational Physics*, Vol. 210, pp. 554-583, 2005.

[31] B. Costa and W. S. Don, "High order hybrid central WENO finite difference scheme for conservation laws". *Journal of Computational and Applied Mathematics*, Vol. 204, pp. 209-218, 2007.

[32] L. Jiang, H. Shan and C. Liu, "Weighted compact scheme for shock capturing". *International Journal of Computational Fluid Dynamics*, Vol. 15, pp. 147-155, 2001.

[33] Y. Ren,M. Liu and H. Zhang, "A characteristic-wise hybrid compact-WENO scheme for solving hyperbolic conservation laws". *Journal of Computational Physics*, Vol. 192, pp. 365-386, 2003,.

[34] A. Bhagatwala and S. K. Lele, "A modified artificial viscosity approach for compressible turbulence simulations". *Journal of Computational Physics*, Vol. 228, pp. 4965-4969.

[35] A. Harten, "High resolution schemes for hyperbolic conservation laws". *Journal of Computational Physics*, Vol. 49, pp. 357-393, 1983.

[36] A. Harten, "The artificial compression method for computation of shocks and contact discontinuities: III. Self-adjusting hybrid schemes". *Mathematics of Computation*, Vol. 32, pp. 363-389, 1978.

[37] A. W. Cook and W. H. Cabot, "A high-wave number viscosity for high-resolution numerical methods". *Journal of Computational Physics*, Vol. 195(2), pp. 594-601, 2004.

[38] B. Cockburn, "Discontinuous Galerkin methods". *Journal of Applied Mathematics and Mechanics*, Vol. 11, pp. 731-754, 2003.

[39] C. L. Streett and M. G. Macaraeg, "Spectral Multidomain for Large-Scale Fluid Dynamic Simulations". *Int. J. Appl. Numer. Math.*, Vol. 6, pp. 123-139, 1989.

[40] C. Liu, H. Fu and P. Lu, "New Shock Detector and Improved Control Function for Shock and Shock-boundary Layer Interaction". *International Journal of Numerical Analysis and Modeling*, Vol. 9(2), pp. 276-288.

[41] C. W. Shu, "Essentially non-oscillatory and weighted essentially non-oscillatory schemes for hyperbolic conservation laws". *NASA techical report 870251*, 1997.

[42] D. A. Kopriva, *Implementing Spectral Methods for Partial Differential Equations*. Springer, 2009.

[43] D. Givoli, "Non-reflecting boundary conditions". *J. Compu. Phys*, Vol. 94, pp. 1-29, 1991.

[44] F. P. Mariano, L. Q. Moreira and A. da Silveira Neto, "Mathematical modeling of non-periodic flows using Fourier pseudo-spectral and immersed boundary methods". *V European Conference on Computational Fluid Dynamics*, J. C. F. Pereira and A. Sequeira (Eds) Lisbon, Portugal, pp. 14?C17, June 2010.

[45] G. A. Sod, "A survey of several finite difference methods for systems on nonlinear hyperbolic conservation laws". *Journal of Computational Physics*, Vol. 27(1), pp. 1-31.

[46] G. D. Bergland, *A Guided Tour of the Fast Fourier Transform*. IEEE Spectrum, Vol. 6, pp. 41-52, 1969.

[47] G. Stipcich, H. Fu and C. Liu, "High-order Mixed Weighted Compact and Non-Compact Scheme for Shock and Small Length Scale Interaction". *International Journal of Computer Mathematics*, Vol. 90(2), pp. 376-407, 2013.

[48] G. Strang, "Wavelet Transforms Versus Fourier Transforms". *Bull. Amer. Math. Soc.*. Vol. 28, pp. 288-305, 1993.

[49] H. Fu and C. Liu, "A Buffered Fourier Spectral Method for Non-periodic PDE". *International Journal of Numerical Analysis and Modeling*, Vol. 9, pp. 460-478, 2012.

[50] H. Fu and C. Liu, "Modified Fourier Spectral Method for Non-periodic CFD". *AIAA conference*, 2012.

[51] H. Fu, Z. Wang, C. Liu and Y. Yan, " Modified Weighted Compact Scheme for Shock Capturing", *Computers and Fluids*, preprint, 2013.

[52] H. Fu, P. Lu and C. Liu, "Improvement of Mixing Function for Modified Upwinding Compact". *AIAA conference*, 2011.

[53] J. D. Anderson, *Computational fluid dynamics*. New York: McGraw Hill, 1995.

[54] J. Steger and R. Warming, "Flux vector splitting of the inviscid gasdynamic equations with applications to finite-difference methods". *Journal of Computational Physics*, Vol. 40, pp. 263-293, 1981.

[55] J. W. Cooley and O. W. Tukey, "An Algorithm for the Machine Calculation of Complex Fourier Series". *Mathematics of Computation*, Vol. 19, pp. 297-301, 1965.

[56] J. D. Fenton and M. M. Rienecker, "A Fourier method for solving nonlinear water-wave problems: application to solitary-wave interactions". *J. Fluid Mech*, Vol.118, pp. 411-443, 1982.

[57] K. Sengupta and F. Mashayek, "Direct Numerical Simulation of Turbulent Flows Using Spectral Methods". *46th AIAA Aerospace Sciences Meeting and Exhibit*, Reno, Nevada, 2008.

[58] M. L. Oliveira, *High-order numerical schemes for high-speed flows*. PhD dissertation, Mathematics dept., University of Texas at Arlington, Arlington, TX, 2009.

[59] R. Vichnevetsky and J. B. Bowles, *Fourier analysis of numerical approximations of hyperbolic equations*. Philadelphia: SIAM, 1982.

[60] S. N. Yu, S. Zhao and G. W. Wei, "Local spectral time splitting method for first and second order partial differential equations". *J. Comp. Phys.*. Vol. 206, pp. 727-780, 2005.

[61] U. Ghia, K. N. Ghia, "High-Re solutions for incompressible flow using the Navier-Stokes equations and a multigrid method". *Journal of Computational Physics*, Vol. 48, pp. 387-411, December 1982.

[62] W. Lyons, H. D. Ceniceros, S. Chandrasekaran and M. Gu, "Fast algorithms for spectral collocation with non-periodic boundary conditions". *Journal of computational physics*, Vol. 207, pp. 173-191, 2005.

[63] W. Press, B. Flannery, S. Teukolsky and W. Vetterling, *Numerical recipes: The art of scientific computing (Fortran Version)*. Cambridge University Press, 1990.

[64] Y. Agnon and H. B. Bingham, "A non-periodic spectral method with application to nonlinear water waves". *Eur. J. Mech. B/Fluids*, Vol. 18(3), pp. 527-534, 1999.

[65] Y. C. Zhou, Y. Gu and G.W. Wei, "Shock-capturing with natural high frequency oscillations". *Int. J. Numer. Methods Fluid*, Vol. 4, pp. 1319-1338, 1997.

[66] Y. Guo, "A new Fourier spectral method for the direct numerical simulation of three-dimensional, spatially growing compressible boundary layer transition". *Technical Report IB 221-93A16*, DLR Gottingen, Germany, 1993.

[67] Y. Sun, Y. C. Zhou, S. Li and G. W. Wei, "A windowed Fourier pseudospectral method for hyperbolic conservation laws". *Journal of Computational Physics*, Vol. 214(2), pp. 466-490.

[68] P. Woodward and P. Colella, "The Numerical Simulation of Two-Dimensional Fluid Flow with Strong Shocks", *Journal of computational physics*, Vol. 54, pp. 115-173, 1984.

[69] C. Liu, P. Lu, M. Oliveira and P. Xie, "Modified Upwinding Compact Scheme for Shock and Shock Boundary Layer Interaction", *Commun. Comput. Phys.,* Vol. 11(3), pp. 1022-1042, 2012.

BIOGRAPHICAL STATEMENT

Huankun Fu was born in Xinghua, Jiangsu Province, China, in 1981. He received his B.S. degree from Xuzhou Normal University, Xuzhou, China, in 2004, his M.S. degrees was from Nanjing University of Aeronautics and Astronautics, and Ph.D. degree from The University of Texas at Arlington in 2013. His research in The University of Texas at Arlington earned him a Stephen R. Bernfeld Memorial Scholarship in 2012. His research interests include numerical methods and their applications in CFD.